

Indirect NMR detection via proton of nuclei subject to large anisotropic interactions, such as ^{14}N , ^{195}Pt , and ^{35}Cl , using the T-HMQC sequence

Cite as: J. Chem. Phys. **156**, 064202 (2022); <https://doi.org/10.1063/5.0082700>

Submitted: 17 December 2021 • Accepted: 18 January 2022 • Published Online: 14 February 2022

 Racha Bayzou,  Julien Trébosc,  Ivan Hung, et al.



View Online



Export Citation



CrossMark

ARTICLES YOU MAY BE INTERESTED IN

[On the potential of Fourier-encoded saturation transfers for sensitizing solid-state magic-angle spinning NMR experiments](#)

The Journal of Chemical Physics **156**, 054201 (2022); <https://doi.org/10.1063/5.0076946>

[Efficient and sideband-free \$^1\text{H}\$ -detected \$^{14}\text{N}\$ magic-angle spinning NMR](#)

The Journal of Chemical Physics **151**, 154202 (2019); <https://doi.org/10.1063/1.5126599>

[Theory and simulations of homonuclear three-spin systems in rotating solids](#)

The Journal of Chemical Physics **155**, 084201 (2021); <https://doi.org/10.1063/5.0055583>

Learn More

The Journal of Chemical Physics **Special Topics** Open for Submissions

Indirect NMR detection via proton of nuclei subject to large anisotropic interactions, such as ^{14}N , ^{195}Pt , and ^{35}Cl , using the T-HMQC sequence

Cite as: J. Chem. Phys. 156, 064202 (2022); doi: 10.1063/5.0082700

Submitted: 17 December 2021 • Accepted: 18 January 2022 •

Published Online: 14 February 2022









View Online



Export Citation



CrossMark

Racha Bayzou,¹  Julien Trébosc,²  Ivan Hung,³  Zhehong Gan,³  Olivier Lafon,^{1,a)} 
and Jean-Paul Amoureux^{1,4,5,a)} 

AFFILIATIONS

¹ Univ. Lille, CNRS, Centrale Lille, Univ. Artois, UMR 8181–UCCS–Unité de Catalyse et Chimie du Solide, 59000 Lille, France

² Univ. Lille, CNRS, INRAE, Centrale Lille, Univ. Artois, FR 2638–IMEC–Fédération Chevreul, 59000 Lille, France

³ National High Magnetic Field Laboratory, 1800 East Paul Dirac Drive, Tallahassee, Florida 32310, USA

⁴ Riken NMR Science and Development Division, Yokohama-shi 230-0045, Kanagawa, Japan

⁵ Bruker Biospin, 34 rue de l'industrie, 67166 Wissembourg, France

^{a)} Authors to whom correspondence should be addressed: olivier.lafon@univ-lille.fr and jean-paul.amoureux@univ-lille.fr

ABSTRACT

Recently, the T-hetero-nuclear multiple quantum coherence (T-HMQC) sequence using the TRAPDOR (transfer of population in double resonance) recoupling has been introduced for the indirect detection via protons of quadrupolar nuclei with spin $I = 1$ (^{14}N) or $3/2$ (^{35}Cl) in solids at fast magic-angle spinning (MAS). The sequence is simple as it only uses four rectangular pulses and exhibits low t_1 -noise because the recoupling pulses are applied to the indirectly detected isotope, I . We demonstrate that this sequence is applicable for the detection via protons of spin-1/2 nuclei subject to large chemical shift anisotropy, such as ^{195}Pt . We also report the proton detection of double-quantum (2Q) coherences of ^{14}N nuclei using this sequence. This 2Q version is more robust to the adjustment of the magic angle and the instabilities of the MAS frequencies than its parent single-quantum (1Q) version since the 2Q coherences are not broadened by the first-order quadrupole interaction. In practice, than its 1Q counterpart for the indirect detection of ^{14}N nuclei, the 2Q variant benefits from a slightly higher resolution and comparable sensitivity. In this article, we derive for the first time the Hamiltonian that describes the spin dynamics during the TRAPDOR recoupling. This Hamiltonian demonstrates the importance of the adiabaticity parameter as well as the role of third-order terms in the effective Hamiltonian. The effects of offsets, radio-frequency field, and recoupling time on the efficiency of the T-HMQC sequence are analyzed numerically as well as with experimental detection via protons of ^{195}Pt nuclei in a mixture of cis- and trans-platin and that of ^{14}N and ^{35}Cl isotopes in L-histidine HCl.

Published under an exclusive license by AIP Publishing. <https://doi.org/10.1063/5.0082700>

I. INTRODUCTION

Solid-state nuclear magnetic resonance (NMR) provides unique insights into the atomic-level structure and dynamics of solids, including membrane proteins, pharmaceuticals, and advanced materials.¹ However, NMR spectra of some isotopes in solids can feature broad powder patterns with breadths ranging from hundreds of kilohertz to tens of megahertz.^{2,3} For

instance, the NMR spectra of paramagnetic or conductive solids are broadened by the hyperfine interactions between unpaired or conduction electrons and nuclei.⁴ In addition, over 74% of the NMR-active isotopes have a spin quantum number $I \geq 1$ and are subject to the quadrupole interactions, which widen their powder spectra, often over several megahertz.⁵ Furthermore, the electron cloud of spin-1/2 nuclei with high atomic numbers, such as ^{119}Sn , ^{195}Pt , ^{199}Hg , or ^{207}Pb , is highly anisotropic, which leads to

wide powder patterns broadened by large chemical shift anisotropy (CSA).³

These isotopes subject to large anisotropic NMR interactions have been first analyzed with direct detection, i.e., their signals were recorded during the acquisition period. However, the direct detection of wide spectra is plagued by several difficulties, such as the experimental dead time. Furthermore, for these isotopes, a major challenge is the lack of sensitivity since these large anisotropic interactions spread the total integrated intensity over a broad spectral width. Several techniques have been proposed to enhance the sensitivity of wide spectra, including (i) the acquisition of multiple echoes using the CPMG (Carr–Purcell Meiboom–Gill) sequence or its variant for half-integer spin quadrupolar nuclei, called QCPMG (quadrupolar CPMG);^{6–8} (ii) the transfer of polarization from protons to the detected isotope using broadband cross-polarization (CP),^{3,9,10} which can be combined with dynamic nuclear polarization (DNP) in order to enhance further the sensitivity;^{11,12} and (iii) in the case of half-integer spin quadrupolar nuclei, the irradiation of the satellite transitions (STs) in order to enhance the signal of the central transition (CT) between energy levels $m_I = \pm 1/2$.¹³ The excitation bandwidth of (Q)CPMG and CP can be improved by the use of adiabatic pulses.^{9,10,14–16} Another difficulty is that the breadth of the NMR spectrum can exceed the detection bandwidth of the probe or the excitation bandwidth of the radio-frequency (rf) pulse, thus requiring a piecewise acquisition called VOCS (variable offset cumulative spectrum).¹⁷

More recently, the indirect detection of wide spectra via one spin-1/2 nucleus, such as ^1H or ^{13}C , has been proposed. In these experiments, the frequencies of the isotope subject to large anisotropic interactions are encoded during the indirect evolution period, t_1 . This approach has been first demonstrated for the observation of ^{14}N nuclei in solids.^{18–20} This nitrogen isotope is the most abundant with a natural abundance $NA = 99.64\%$. However, because of its integer spin value, $I = 1$, all its single-quantum (1Q) transitions are broadened by the first-order quadrupole interaction (H_{Q1}), and ^{14}N powder patterns with a width of up to 10.5 MHz have been reported.²¹ ^{14}N 1Q or double-quantum (2Q) coherences can be indirectly detected using two-dimensional (2D) hetero-nuclear correlation (HETCOR) sequences, such as HMQC or HSQC (hetero-nuclear multiple- or single-quantum coherence), with coherence transfers mediated by either residual dipolar splitting (which is the sum of J -coupling and second-order quadrupole–dipole cross-terms)^{18–20,22,23} or dipolar interactions.^{24,25} In the latter approach, called D -HMQC or D -HSQC, the dipolar interactions between the spy spins and the ^{14}N isotope are reintroduced under magic-angle spinning (MAS) by applying a hetero-nuclear dipolar recoupling sequence to the spy spins. In the case of proton detection, denoted $^1\text{H}\{-^{14}\text{N}\}$ hereafter, $^1\text{H}\{-^{14}\text{N}\}$ dipolar couplings are generally reintroduced by applying the symmetry-based SR4_1^2 recoupling, which also suppresses the contribution of $^1\text{H}\{-^1\text{H}\}$ dipolar interactions to the first-order average Hamiltonian and offers tolerance to rf inhomogeneity.²⁶ The HMQC sequence is more sensitive than the HSQC one.^{23,27} The indirect detection of ^{14}N 1Q coherences requires a very stable spinning precisely at the magic angle, $\beta_{\text{RL}} \approx 54.736^\circ$, in order to average out H_{Q1} . Conversely, the ^{14}N 2Q coherences between energy levels $m_I = \pm 1$ are not broadened by H_{Q1} , and hence, their indirect detection does not require a precise adjustment and a high stability of the magic angle and

the spinning frequency, ν_{R} .¹⁸ Nevertheless, the indirect detection of ^{14}N 2Q coherences is usually less efficient than that of 1Q ones.^{25,28–30}

A challenge for the indirect detection of ^{14}N nuclei using HMQC or HSQC sequences is that the ^{14}N rf-amplitude is limited to a few tens of kilohertz, which is two orders of magnitude lower than the ^{14}N H_{Q1} interaction. Various schemes applied at the ^{14}N Larmor frequency have been proposed for the excitation and the reconversion of ^{14}N 1Q and 2Q coherences. They include hard pulses using high rf-power,¹⁹ sideband selective long pulses (SLPs),^{20,28} trains of short rotor-synchronized DANTE (delays alternating with nutation for tailored excitation) pulses,^{31,32} or low-power rotor-synchronized symmetry-based sequences, including XiX (X inverse X) pulse trains.^{30,33,34} We notably showed that SLPs are advantageous because they are efficient, robust, and easy to set up.³⁰ The overtone irradiation and detection at twice the ^{14}N Larmor frequency with rectangular, composite, or adiabatic pulses has also been employed in HMQC experiments, but it is less effective than irradiation at the ^{14}N Larmor frequency.^{29,35–38}

Nevertheless, an important limitation of the $^1\text{H}\{-^{14}\text{N}\}$ D -HMQC sequence [Fig. 1(a)] using coherence transfers mediated by dipolar couplings is the important t_1 -noise, appearing as spurious streaks along the indirect dimension, F_1 . This noise reduces the sensitivity and can mask true cross peaks of low intensity, thus hampering a reliable interpretation of the 2D spectra.^{39,40} This t_1 -noise mostly stems from the random fluctuations of the MAS frequency.⁴⁰ The SR4_1^2 recoupling reintroduces the ^1H CSA, besides the $^1\text{H}\{-^{14}\text{N}\}$ dipolar interaction, and is non- γ -encoded. Because of the instabilities, the defocusing and refocusing periods of the D -HMQC sequence are not always perfectly rotor-synchronized, and hence, the amplitude of the recoupled ^1H CSA differs between these two delays, which results in its imperfect refocusing and hence, in a variation in signal amplitude from scan to scan. Owing to these variations, the uncorrelated signal is not perfectly canceled by the phase cycling, which leads to t_1 -noise. Different approaches have been proposed to reduce this limitation. It has been demonstrated that short recycle delays decrease the t_1 -noise, which is coherent and hence

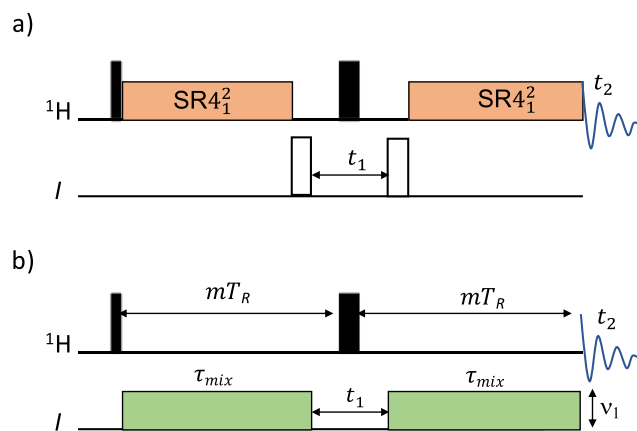


FIG. 1. $^1\text{H}\{-I\}$ (a) D -HMQC and (b) T-HMQC pulse sequences. The $^1\text{H}\{-I\}$ dipolar couplings are reintroduced by applying either the SR4_1^2 recoupling on the ^1H channel for D -HMQC or two long identical pulses on the I channel for T-HMQC.

proportional to the signal amplitude.⁴¹ The t_1 -noise in the D -HMQC or D -HSQC spectra using the SR4₁ recoupling can also be decreased by inserting two simultaneous π -pulses on ^1H and indirect channels in the middle of the defocusing and refocusing periods in order to refocus the ^1H CSA.⁴⁰ These variants have been called TONE (t_1 -noise eliminated) D -HMQC or D -HSQC sequences. However, an efficient inversion of the ^{14}N magnetization using short pulses requires a high rf-power that is not compatible with the specifications of most NMR probes,^{33,42–46} and the TONE approach has not been reported so far for the indirect detection of ^{14}N nuclei via protons. The t_1 -noise of $^1\text{H}\{-^{14}\text{N}\}$ D -HMQC 2D spectra can also be reduced by employing a γ -encoded scheme, such as the rotary resonance recoupling (R^3), which is more tolerant to MAS frequency fluctuations because the desynchronization of the defocusing and refocusing periods does not change the amplitude of the recoupled interactions but only their phase.^{24,47} Nevertheless, the R^3 scheme is sensitive to rf-inhomogeneity, notably for protons subject to small CSA.

Alternatively, the $^1\text{H}\text{-}^{14}\text{N}$ dipolar interactions can be reintroduced in HMQC experiments by applying two long identical pulses on the ^{14}N channel,^{48–51} like in the TRAPDOR (transfer of population in double resonance) experiment.^{52–54} This combination of the TRAPDOR and HMQC schemes has been called T-HMQC.⁵¹ These long pulses also excite and reconvert the ^{14}N coherences evolving during the t_1 period. As these long pulses are applied to the ^{14}N channel, they do not reintroduce the ^1H CSA, and hence, the T-HMQC 2D spectra do not feature any t_1 -noise.⁵¹ To the best of our knowledge, this scheme has so far been applied for the indirect detection of ^{14}N 1Q coherences, but not of their 2Q ones.

The NMR signal of the ^{14}N isotope can also be detected via protons under MAS using the double cross-polarization sequence.^{51,55,56} Nevertheless, this sequence requires a careful optimization of the rf-fields on ^1H and ^{14}N channels during the CP transfers in order to fulfill the Hartmann–Hahn condition⁵⁵ while avoiding the R^3 ones.⁵¹

Half-integer spin quadrupolar nuclei, including ^{17}O , ^{23}Na , ^{25}Mg , ^{27}Al , ^{35}Cl , ^{43}Ca , and ^{71}Ga , have also been indirectly detected by protons.^{27,57–61} This indirect detection has been achieved using either the D -HMQC sequence^{57–61} and its TONE variant⁴⁰ or, more recently, the magnetization transfers between half-integer quadrupolar nuclei and protons using the D -RINEPT (through-space refocused insensitive nuclei enhanced by polarization transfer) scheme.⁶¹ It has notably been demonstrated that the D -HMQC sequence allows the indirect detection of the 1Q-CT and 1Q-ST coherences of ^{35}Cl nucleus,⁵⁸ which is a spin-3/2 isotope with a low gyromagnetic ratio ($\gamma_{^{35}\text{Cl}}/\gamma_{^1\text{H}} = 0.098$) and high natural abundance ($NA = 75.77\%$). More recently, the T-HMQC experiment has been employed for the indirect detection via protons of either the 1Q (1Q-CT and 1Q-ST) and triple-quantum (3Q) coherences of ^{35}Cl nuclei or the 2Q-ST ones between energy levels $m_I = \pm 3/2$ and $\mp 1/2$ of this quadrupolar isotope.⁶² The detection of 1Q-ST and 2Q-ST requires a very stable spinning (within a few Hz) precisely at the magic angle (within a few milli-degrees) in order to average H_{Q1} . These requirements are called STMAS specifications.^{63–66} When they are met, the indirect detection of the 2Q-ST can improve the resolution by a factor of up to 18 over that of the 1Q-CT.

D -HMQC experiments with ^1H detection and its TONE variants have also been applied for the indirect detection of ^{195}Pt nuclei in solids.^{59,67–70} ^{195}Pt is a spin-1/2 isotope with a moderate gyromagnetic ratio ($\gamma_{^{195}\text{Pt}}/\gamma_{^1\text{H}} \approx 0.215$) and natural abundance ($NA = 33\%$). ^{195}Pt CSA can exceed 7000 ppm, leading to spectral breadths larger than 500 kHz at 9.4 T.⁷¹ Therefore, the excitation of ^{195}Pt nuclei using rf-amplitudes of tens of kilohertz is challenging. This excitation has been performed using various schemes, including hard pulses, SLPs, and DANTE trains.⁶⁸ SLP is notably suitable for large CSA. The MAS sideband manifold of ^{195}Pt nuclei can also be recorded using rotor-asynchronous t_1 -increments in a constant-time D -HMQC sequence⁵⁹ or preferably its variant with arbitrary dwell time.^{70,72} The ^1H signal can also be correlated with the ^{195}Pt center-band by combining the D -HMQC sequence with the adiabatic magic-angle turning scheme.^{67,70} Nevertheless, the acquisition of two D -HMQC 2D spectra with different spinning speeds using rotor-synchronized t_1 -increments is sufficient to determine the isotropic chemical shifts of ^{195}Pt nuclei.⁶⁸

We demonstrate herein the indirect detection of 2Q ^{14}N coherences via protons using the T-HMQC sequence. We show for the first time that the T-HMQC experiment can be applied for the indirect observation of spin-1/2 nuclei, such as ^{195}Pt , subject to large CSA. We also analyze the efficiency of the $^1\text{H}\{-I\}$ T-HMQC sequence for $I = ^{14}\text{N}$, ^{35}Cl , and ^{195}Pt isotopes as a function of offset, recoupling time, and rf-amplitude using spin dynamics simulations. The $^1\text{H}\{-^{14}\text{N}\}$ and $^1\text{H}\{-^{35}\text{Cl}\}$ T-HMQC experiments are carried out on L-histidine HCl, whereas the $^1\text{H}\{-^{195}\text{Pt}\}$ ones are performed on a mixture of *cis*- and *trans*-dichlorodiamineplatinum(II) (also called *cis*-platin and *trans*-platin).

II. PULSE SEQUENCE AND THEORY

A. Pulse sequence

The $^1\text{H}\{-I\}$ T-HMQC pulse sequence is displayed on Fig. 1(b). It consists of a rotor-synchronized spin-echo on the ^1H channel, i.e., the interval between the centers of the $\pi/2$ and π pulses and that between the center of the π -pulse and the beginning of the acquisition period, t_2 , are equal to an integer multiple of rotor periods, mT_R . Two long rectangular pulses of identical length, τ_{mix} , and rf-strength, ν_1 , are applied on the I channel during each echo delay and are separated by the t_1 evolution period. This pair of long pulses reintroduces the $^1\text{H}\text{-}I$ dipolar coupling under MAS and also creates and reconverts the I coherences evolving during the t_1 period in order to encode their frequency.

The phase cycling of one of these I pulses allows selecting the coherence order during t_1 . In the following, we will label the coherences according to their coherence order either followed by ST when they are subject to H_{Q1} (e.g., 1Q-ST and 2Q-ST) or without ST in other cases (e.g., 1Q-CT and 3Q for $I = 3/2$).

A two-step phase cycle selects simultaneously all coherences with odd order of the I isotope. This means that only the $\pm 1\text{Q}$ coherences can then be detected for ^{195}Pt and ^{14}N isotopes owing to the limited sizes of their density matrices stemming from their small spin values: $I = 1/2$ and 1, respectively, whereas this phase cycling selects simultaneously 1Q-CT, 1Q-ST, and 3Q for $I = 3/2$.

Conversely, a four-step phase cycle selects the $\pm 2\text{Q}$ coherences and notably the 2Q-ST for $I = 3/2$.⁶² For this spin value, the

second-order quadrupolar (H_{Q2}) broadening of the 2Q-ST in hertz is ninefold smaller than that of 1Q-CT, whereas the differences in chemical shifts for the former coherences are twice larger than for the latter.⁶² Overall, the spectral resolution is hence improved by a factor of 18 by selecting the 2Q-ST instead of 1Q-CT during the t_1 period. However, the 2Q-ST is broadened by H_{Q1} , and hence, this phase selection requires STMAS specifications to cancel this broadening. For $I = 1$, the 1Q and 2Q coherences lead to the same resolution, provided they only evolve under the isotropic chemical shift and H_{Q2} interactions. However, the 1Q coherences are also subject to H_{Q1} , which is only refocused under STMAS specifications. Conversely, the 2Q coherences are immune to H_{Q1} and does not require these stringent settings.

A six-step phase cycle selects the $\pm 3Q$ coherences during t_1 . For $I = 3/2$, the 3Q coherences are not broadened by H_{Q1} , and hence, their indirect detection does not require STMAS specifications.

B. Effective TRAPDOR Hamiltonian for $I = 1/2$

We consider a rectangular pulse of phase x applied under MAS to the ^{195}Pt nucleus with a carrier frequency resonant with its n th-order sideband related to CSA. We neglect the off-resonance counter-rotating circular component of the linearly modulated rf-field. In the rotating frame, \mathcal{R} , revolving around the z -axis of the laboratory frame at $\delta_{\text{iso}}^I \omega_I^0$, where δ_{iso}^I and ω_I^0 denote, respectively, the isotropic chemical shift and the Larmor angular frequency, the Hamiltonian of an isolated pair $S = ^1\text{H}$ and $I = ^{195}\text{Pt}$ can be expressed as

$$H^{\mathcal{R}} = \omega_{\text{CSA},I}(t)I_z + 2\omega_{\text{D},IS}(t)I_z S_z + \omega_1 R_z(n\omega_{\text{R}}t)I_x R_z(-n\omega_{\text{R}}t), \quad (1)$$

where $R_z(\theta) = \exp(-i\theta I_z)$ is the operator for the rotation of the ^{195}Pt spin through an angle θ around the z -axis, $\omega_{\text{R}} = 2\pi\nu_{\text{R}}$ is the angular MAS frequency, $\omega_{\text{CSA},I}(t)$ is the instantaneous angular frequency of the ^{195}Pt CSA, $\omega_{\text{D},IS}(t)$ is the instantaneous angular dipolar coupling frequency, and $\omega_1 = 2\pi\nu_1$ is the amplitude of the rf-field.

The ^{195}Pt CSA is usually much larger than the ^1H - ^{195}Pt dipolar coupling. Its MAS-modulated offset can be removed by a transformation into the jolting frame, \mathcal{J} ,⁷³

$$H^{\mathcal{J}} = R_z[-\Phi_{\text{CSA},I}(t)]H^{\mathcal{R}}R_z[\Phi_{\text{CSA},I}(t)] - \omega_{\text{CSA},I}(t)I_z, \quad (2)$$

where

$$\Phi_{\text{CSA},I}(t) = \int_0^t \omega_{\text{CSA},I}(t') dt' \quad (3)$$

is the phase related to the evolution under ^{195}Pt CSA. MAS modulates the ^{195}Pt CSA and ^1H - ^{195}Pt dipolar interaction at the frequency ω_{R} . Hence, the Hamiltonian $H^{\mathcal{J}}$ can be expressed as³³

$$H^{\mathcal{J}} = \sum_{p=-\infty}^{+\infty} \left[2\omega_p^{D,IS} I_z S_z + h_p^{\text{rf}} \right] \exp(ip\omega_{\text{R}}t), \quad (4)$$

where the complex amplitudes of the components of the ^1H - ^{195}Pt dipolar interaction are equal to⁷⁴

$$\omega_{\pm 1}^{D,IS} = \mp \frac{1}{2\sqrt{2}} b_{IS} \sin(2\beta_{PR}^{D,IS}) \exp[\mp i(\gamma_{PR}^{D,IS} + \alpha_{RL}^0)], \quad (5)$$

$$\omega_{\pm 2}^{D,IS} = \frac{1}{4} b_{IS} \sin^2(\beta_{PR}^{D,IS}) \exp[\mp i2(\gamma_{PR}^{D,IS} + \alpha_{RL}^0)], \quad (6)$$

whereas the other components are null. In Eqs. (5) and (6), b_{IS} is the dipolar coupling in $\text{rad} \cdot \text{s}^{-1}$, $\{0, \beta_{PR}^{D,IS}, \gamma_{PR}^{D,IS}\}$ Euler angles relate the I - S inter-nuclear direction to the MAS rotor-fixed frame, and α_{RL}^0 denotes the rotor angular position at the beginning of the pulse. The Floquet coefficients of the rf Hamiltonian have the following expression:³³

$$h_p^{\text{rf}} = \frac{\omega_1}{2} [A_{n-p} \exp(-i\phi_{n-p}) I_- + A_{n+p} \exp(i\phi_{n+p}) I_+], \quad (7)$$

where $A_{n\pm p}$ and $\phi_{n\pm p}$ are the amplitude and the phase of the $(n \pm p)$ th-order sidebands of the crystallite and I_{\pm} denotes the ladder operators of the ^{195}Pt nucleus. The first-order effective Hamiltonian corresponds to the time-independent term $p = 0$ in Eq. (4) and is equal to the Floquet coefficient h_0^{rf} ,

$$H_{\text{eff}}^{(1)} = h_0^{\text{rf}} = \omega_1 A_n R_z(-\phi_n) I_x R_z(\phi_n), \quad (8)$$

which is identical to the Hamiltonian of a rectangular pulse applied to the ^{195}Pt nucleus with amplitude $\omega_1 A_n$ and phase ϕ_n . The scaling down of the rf-field by A_n stems from the fact that it rotates the magnetization only during a fraction of the pulse since the modulation of CSA by MAS produces a rapid change of the offset. The amplitude A_n and the phase ϕ_n depend on the orientation of the CSA tensor in the rotor frame. This dependence results in a distribution of the rf-strength and a spread of its direction between the crystallites of a powder.

For a large rf-amplitude, higher order terms of the rf Hamiltonian must be included. The second-order effective rf Hamiltonian is equal to^{33,75}

$$H_{\text{eff,rf}\times\text{rf}}^{(2)} = \frac{\omega_1^2}{\omega_{\text{R}}} \sum_{p \neq 0} \frac{A_{n+p}^2 - A_{n-p}^2}{p} I_z. \quad (9)$$

This constant term represents a Bloch-Siegert shift,^{76,77} which does not depend on the phases of the rf-pulse and the spinning sidebands (ϕ_n). Its magnitude increases with $\omega_1^2/\omega_{\text{R}}$ and the asymmetry of the sideband intensities about the irradiated sideband.

As seen in Eqs. (8) and (9), neither $H_{\text{eff}}^{(1)}$ nor $H_{\text{eff,rf}\times\text{rf}}^{(2)}$ depends on b_{IS} and account for the reintroduction of ^1H - ^{195}Pt dipolar coupling by the long pulse, even if, as shown below, these terms do not commute with the recoupled ^1H - ^{195}Pt dipolar interaction and affect the ^1H - ^{195}Pt coherence transfer during the TRAPDOR pulses by modifying the quantization axis. On the contrary, the ^1H - ^{195}Pt dipolar interaction contributes to the second-order effective Hamiltonian via the following term:

$$H_{\text{eff,IS}\times\text{rf}}^{(2)} = -\frac{1}{2} \sum_{p \neq 0} \frac{[2\omega_p^{D,IS} I_z S_z, h_p^{\text{rf}}] + [h_p^{\text{rf}}, 2\omega_p^{D,IS} I_z S_z]}{p\omega_{\text{R}}}. \quad (10)$$

By substituting Eq. (7) into Eq. (10), this Hamiltonian can be written as

$$H_{\text{eff},IS \times \text{rf}}^{(2)} = \frac{\omega_1}{2\omega_R} \sum_{\substack{p=-2 \\ p \neq 0}}^2 \text{sign}(p) \omega_p^{D,IS} [-A_{n+p} \exp(-i\phi_{n+p}) I_- + A_{n-p} \exp(i\phi_{n-p}) I_+] S_z. \quad (11)$$

This equation shows that the rectangular pulse, resonant with the n th-order sideband of ^{195}Pt nucleus, reintroduces the hetero-nuclear dipolar coupling and converts the ^1H IQ coherences into ^1H - ^{195}Pt multiple-quantum coherences evolving during the t_1 period of the T-HMQC sequence.

Equation (11) shows that the amplitude of the $H_{\text{eff},IS \times \text{rf}}^{(2)}$ term governing the ^1H - ^{195}Pt coherence transfer depends on the $\omega_1 A_{n+p} b_{IS} / \omega_R$ ratios, with $p = \pm 1$ and ± 2 . The A_k amplitudes satisfy the normalization conditions,⁷⁸

$$\sum_{k=-\infty}^{+\infty} A_k^2 = 1. \quad (12)$$

Let us call CSA the full width of the static powder pattern,

$$\text{CSA} = \delta_{\text{aniso}}^I \omega_I^0 (3 + \eta_{\text{CSA}}) / 2, \quad (13)$$

where δ_{aniso}^I and η_{CSA} denote the anisotropic chemical deshielding constant and the shielding asymmetry parameter of ^{195}Pt nucleus, respectively. The number of spinning sidebands with significant intensities is approximately equal to CSA / ω_R and hence, in average,

$$A_k \approx \sqrt{\frac{\omega_R}{\text{CSA}}}. \quad (14)$$

Therefore, the norm of $H_{\text{eff},IS \times \text{rf}}^{(2)}$ is approximately proportional to

$$\|H_{\text{eff},IS \times \text{rf}}^{(2)}\| \propto \sqrt{\alpha} b_{IS}, \quad (15)$$

where the adiabaticity parameter, α , is given by

$$\alpha = \frac{\omega_1^2}{\omega_R \text{CSA}}. \quad (16)$$

For $\nu_1 = 186$ kHz and $\nu_R = 62.5$ kHz, corresponding to the experimental conditions used in Sec. IV B and $\delta_{\text{aniso}}^I \omega_I^0 / (2\pi) = 1.02$ MHz and $\eta_{\text{CSA}} = 0.03$ ($\text{CSA} = 1.55$ MHz), which are the CSA parameters of ^{195}Pt nucleus in cis-platin,⁵⁹ we have $\alpha \approx 0.36$. Therefore, the buildup of the T-HMQC signal, which is proportional to $\sqrt{\alpha}$ [Eq. (15)], is accelerated at a higher rf-field, whereas it is slowed down at larger CSA and higher MAS frequency.

Furthermore, the magnitude of $H_{\text{eff}}^{(1)} = h_0^{\text{rf}}$ is much larger than that of $H_{\text{eff},IS \times \text{rf}}^{(2)}$. In the interaction frame of h_0^{rf} , the effective Hamiltonian is equal to

$$H^{h_0}(t) = \exp(ih_0^{\text{rf}} t) \left(H_{\text{eff},\text{rf} \times \text{rf}}^{(2)} + H_{\text{eff},IS \times \text{rf}}^{(2)} \right) \exp(-ih_0^{\text{rf}} t). \quad (17)$$

The terms of $H_{\text{eff},\text{rf} \times \text{rf}}^{(2)} + H_{\text{eff},IS \times \text{rf}}^{(2)}$ which do not commute with h_0^{rf} , oscillate rapidly and are averaged out by the rf-field. Therefore, the recoupling of the ^1H - ^{195}Pt dipolar interaction is governed by the projection of $H_{\text{eff},IS \times \text{rf}}^{(2)}$ onto $h_0^{\text{rf}} S_z$,

$$H_{\text{eff},IS \times \text{rf}}^{(2),h_0} = \frac{\text{Tr}(S_z h_0^{\text{rf},\dagger} H_{\text{eff},IS \times \text{rf}}^{(2)})}{\text{Tr}(S_z h_0^{\text{rf},\dagger} h_0 S_z)} h_0^{\text{rf}} S_z, \quad (18)$$

where $h_0^{\text{rf},\dagger}$ denotes the Hermitian adjoint of h_0^{rf} and $\text{Tr}(B)$ denotes the trace of matrix B . The magnitude of this term is proportional to $\sqrt{\alpha}$, and depends on the sideband intensities, $A_{n \pm p}$, and phases, $\phi_{n \pm p}$, with $p = \pm 1$ or ± 2 .

C. Effective TRAPDOR Hamiltonian for $I = 1$

We now consider the case of the ^1H - $\{^{14}\text{N}\}$ T-HMQC pulse sequence. Two rectangular pulses of phase x are applied under MAS to the ^{14}N nucleus with a carrier frequency resonant with the n th and $-n$ th order sidebands of the transitions between energy levels $+1 \leftrightarrow 0$ and $0 \leftrightarrow -1$, respectively. In the case of an isolated spin pair, $S = ^1\text{H}$ and $I = ^{14}\text{N}$, the Hamiltonian in the \mathcal{R} rotating frame is equal to

$$H^{\mathcal{R}}(t) = \omega_{Q,I}(t) Q_z + 2\omega_{D,IS}(t) I_z S_z + \omega_1 R_z(n\omega_R t) I_x R_z(-n\omega_R t), \quad (19)$$

where $Q_z = I_z^2 - I(I+1)\mathbf{1}_I/3$ is the quadrupolar order, $\mathbf{1}_I$ is the identity matrix of size $2I+1 = 3$, and $\omega_{Q,I}(t)$ is the instantaneous H_{Q1} interaction. In Eq. (19), we disregarded the CSA and the anisotropic part of H_{Q2} , since they are usually smaller than the MAS frequency. Furthermore, the isotropic part of H_{Q2} , also called QIS (quadrupolar-induced shift), ω_{QIS}^I , is included in the frequency offset of the ^{14}N nucleus and the \mathcal{R} frame revolves around the z -axis of the laboratory frame at the angular frequency, $\delta_{\text{iso}}^I \omega_I^0 + \omega_{QIS}^I$.

As H_{Q1} of the ^{14}N nucleus is usually much larger than the ^1H - ^{14}N dipolar coupling, the Hamiltonian is transformed into the quadrupolar jolting frame, \mathcal{J} , in order to remove its modulation by MAS,

$$H^{\mathcal{J}}(t) = \exp[i\Phi_{Q,I}(t) Q_z] H^{\mathcal{R}} \exp[-i\Phi_{Q,I}(t) Q_z] - \omega_{Q,I}(t) Q_z, \quad (20)$$

where

$$\Phi_{Q,I}(t) = \int_0^t \omega_{Q,I}(t') dt' \quad (21)$$

is the phase evolution under H_{Q1} . Owing to the periodicity of the MAS rotation, the Hamiltonian $H^{\mathcal{J}}$ can be written as in Eq. (4),³³ in which the Floquet coefficients of the rf Hamiltonian are given by

$$h_p^{\text{rf}} = \sqrt{\frac{1}{2}} \omega_1 \left[\begin{array}{l} A_{n-p} \exp(-i\phi_{n-p}) I_{-}^{(+1,0)} + A_{n+p} \exp(i\phi_{n+p}) I_{+}^{(+1,0)} \\ + A_{-n+p} \exp(i\phi_{-n+p}) I_{-}^{(0,-1)} + A_{-n-p} \exp(-i\phi_{-n-p}) I_{+}^{(0,-1)} \end{array} \right], \quad (22)$$

where $I_{\pm}^{(+1,0)}$ and $I_{\pm}^{(0,-1)}$ denote the ladder operators of the transitions $+1 \leftrightarrow 0$ and $0 \leftrightarrow -1$, respectively, and the coefficients of $I_{\pm}^{(\pm 1,0)}$ operators are the complex conjugates of those $I_{\pm}^{(0,\mp 1)}$.

The first-order effective Hamiltonian is the coefficient h_0^{rf} ,

$$H_{\text{eff}}^{(1)} = h_0^{\text{rf}} = \sqrt{2} \omega_1 \left[\begin{array}{l} A_n R_z^{(+1,0)}(-\phi_n) I_x^{(+1,0)} R_z^{(+1,0)}(\phi_n) \\ + A_{-n} R_z^{(0,-1)}(\phi_{-n}) I_x^{(0,-1)} R_z^{(0,-1)}(-\phi_{-n}) \end{array} \right], \quad (23)$$

where $R_z^{(+1,0)}(\theta) = \exp(-i\theta I_z^{(+1,0)})$ and $R_z^{(0,-1)}(\theta) = \exp(-i\theta I_z^{(0,-1)})$. The above Hamiltonian corresponds to two pulses of distinct amplitudes and phases applied to the transitions $+1 \leftrightarrow 0$ and $0 \leftrightarrow -1$, respectively.

The second-order effective rf Hamiltonian comprises terms proportional to $I_z^{(+1,0)}$ and $I_z^{(0,-1)}$, representing the Bloch–Siegert shift as well as double-quantum terms.³³ By substituting Eq. (23) into Eq. (10), the contribution of the ^1H – ^{14}N dipolar interaction to the second-order effective Hamiltonian can be expressed as

$$H_{\text{eff},IS \times \text{rf}}^{(2)} = \frac{\omega_1}{\sqrt{2} \omega_R} \sum_{p \neq 0}^2 \text{sign}(p) \omega_p^{D,IS} \left[\begin{array}{l} -A_{n+p} \exp(-i\phi_{n+p}) I_{-}^{(+1,0)} + A_{n-p} \exp(i\phi_{n-p}) I_{+}^{(+1,0)} \\ -A_{-n-p} \exp(i\phi_{-n-p}) I_{-}^{(0,-1)} + A_{-n+p} \exp(-i\phi_{-n+p}) I_{+}^{(0,-1)} \end{array} \right] S_z. \quad (24)$$

As h_0^{rf} is much larger than this Hamiltonian, the evolution of the spin system can be described in the h_0^{rf} interaction frame [Eq. (17)] and the transfer of coherence between ^1H and ^{14}N nuclei is governed by the projection of $H_{\text{eff},IS \times \text{rf}}^{(2)}$ onto $h_0^{\text{rf}} S_z$ given by Eq. (18). This effective Hamiltonian transforms the in-phase transverse ^1H magnetization, S_x , into (i) a transverse ^1H magnetization antiphase with respect to ^1H – ^{14}N coupling, $S_x (I_z^2 - \frac{2}{3} I_x)$, as well as (ii) ^1H – ^{14}N multiple-quantum coherences with 1Q and 2Q ^{14}N coherences.

As the full width powder pattern of a I spin nucleus is $1.5C_Q/I$,⁷⁹ in average, we have

$$A_k \approx \sqrt{\frac{I \omega_R}{1.5 C_Q}} \quad (25)$$

using the normalization condition of Eq. (12), and hence, Eq. (15) is still valid with the adiabaticity parameter, α , given by

$$\alpha = \frac{I \omega_1^2}{1.5 \omega_R C_Q}. \quad (26)$$

For ^{14}N nuclei with $\nu_1 = 70$ kHz, $\nu_R = 62.5$ kHz, and $C_Q = 1.18$ MHz, we have $\alpha \approx 0.04 \ll 1$.

In the special case, in which the centerband is irradiated ($n = 0$), the coefficients of $I_{\pm}^{(+1,0)}$ and $I_{\mp}^{(0,-1)}$ operators in Eq. (24) are opposite. As a result, $H_{\text{eff},IS \times \text{rf}}^{(2)}$ is orthogonal to h_0^{rf} , which fully decouples the ^1H – ^{14}N dipolar interaction and cancels the T-HMQC signal.

Furthermore, the third-order effective term between two rf Hamiltonians and the ^1H – ^{14}N dipolar interaction, $H_{\text{eff},IS \times \text{rf} \times \text{rf}}^{(3)}$ [Eq. (S1)], contains products of S_z and ^{14}N 2Q operators.³³

These product operators can transform S_x into ^1H – ^{14}N coherences involving ^{14}N 2Q coherences. As this third-order term is proportional to αb_{IS} and $\alpha \leq \sqrt{\alpha} \leq 1$, its contribution to the creation of ^{14}N 2Q coherences increases with the ^1H – ^{14}N dipolar interaction and the length of the TRAPDOR pulses.

We considered above the irradiation of the n th-order sideband. When irradiating the midpoint between two consecutive spinning sidebands, i.e., the frequency offset is equal to $(n + 1/2)\nu_R$, h_p^{rf} must be replaced by $h_p^{\text{rf}} \exp(i\omega_R t/2)$ in Eq. (4). Hence, the first-order Hamiltonian and the contribution of the ^1H – ^{14}N dipolar interaction to the second-order effective Hamiltonian are time-dependent and canceled by MAS since the rf-field is modulated at a half-integer multiple of the MAS frequency, whereas the H_{Q1} and ^1H – ^{14}N dipolar interactions are modulated at multiples of the MAS frequency. Nevertheless, the third-order effective Hamiltonian of Eq. (S2) contains time-independent terms recoupling the ^1H – ^{14}N dipolar interaction.³³ As this Hamiltonian contains products of S_z and ^{14}N 2Q operators, the irradiation at the midpoint between two consecutive spinning sidebands can transform S_x into ^1H – ^{14}N coherences involving 2Q coherences. As the third-order term is proportional to αb_{IS} and $\alpha \leq \sqrt{\alpha} \leq 1$, the buildup of the ^{14}N 2Q coherences in T-HMQC experiments is slower at these offsets than for the irradiation of a sideband.

D. Effective TRAPDOR Hamiltonian for $I = 3/2$

For the ^1H – $\{^{35}\text{Cl}\}$ T-HMQC sequence, two rectangular pulses of phase x are applied under MAS to the ^{35}Cl channel with a carrier frequency resonant with sidebands of order n and $-n$ of the transitions $3/2 \leftrightarrow 1/2$ and $-1/2 \leftrightarrow -3/2$, respectively. The Hamiltonian of the ^1H – ^{35}Cl spin pair in the \mathcal{R} frame is equal to

$$H^R = \omega_{Q,I}(t)Q_z + 2\omega_{D,IS}(t)I_zS_z + \omega_1R_z(n\omega_R t)I_xR_z(-n\omega_R t) \quad (27)$$

in which the ^{35}Cl CSA and H_{Q2} interactions are disregarded.

The STs of the ^{35}Cl nucleus, $3/2 \leftrightarrow 1/2$ and $-1/2 \leftrightarrow -3/2$, are similar to those of ^{14}N isotope: $+1 \leftrightarrow 0$ and $0 \leftrightarrow -1$,

whereas the ^{35}Cl 1Q-CT coherence does not evolve under H_{Q1} and only contributes to the centerband. By analogy with a spin $I = 1$, it can be shown that the Floquet coefficients of the rf Hamiltonian for $I = 3/2$ in the quadrupolar jolting frame are equal to

$$h_p^{\text{rf}} = \frac{\sqrt{3}}{2}\omega_1 \left[\begin{array}{l} A_{n-p} \exp(-i\phi_{n-p})I_-^{(+\frac{3}{2},+\frac{1}{2})} + A_{n+p} \exp(i\phi_{n+p})I_+^{(+\frac{3}{2},+\frac{1}{2})} \\ + A_{-n+p} \exp(i\phi_{-n+p})I_-^{(-\frac{1}{2},-\frac{3}{2})} + A_{-n-p} \exp(-i\phi_{-n-p})I_+^{(-\frac{1}{2},-\frac{3}{2})} \end{array} \right] + \omega_1 \delta_{n0} \delta_{p0} C_x, \quad (28)$$

where C_x is the 1Q-CT coherence along the x -axis and δ_{n0} and δ_{p0} denote Kronecker delta functions.⁸⁰ Similarly, by analogy with Eq. (24), the contribution of the ^1H - ^{35}Cl dipolar interaction to the second-order effective Hamiltonian is

$$H_{\text{eff},IS \times \text{rf}}^{(2)} = \frac{\sqrt{3}\omega_1}{2\omega_R} \sum_{p_p \neq 0}^2 \text{sign}(p) \omega_p^{D,IS} \left[\begin{array}{l} -A_{n+p} \exp(-i\phi_{n+p})I_-^{(+\frac{3}{2},+\frac{1}{2})} + A_{n-p} \exp(i\phi_{n-p})I_+^{(+\frac{3}{2},+\frac{1}{2})} \\ -A_{-n-p} \exp(i\phi_{-n-p})I_-^{(-\frac{1}{2},-\frac{3}{2})} + A_{-n+p} \exp(-i\phi_{-n+p})I_+^{(-\frac{1}{2},-\frac{3}{2})} \\ -\frac{\text{sign}(p)}{\sqrt{3}} \left(-I_-^{(+\frac{1}{2},-\frac{1}{2})} + I_+^{(+\frac{1}{2},-\frac{1}{2})} \right) \end{array} \right] S_z. \quad (29)$$

The full width of the ^{35}Cl static powder pattern is C_Q ,⁷⁹ and the adiabaticity parameter, α , is given by Eq. (26).

As $H_{\text{eff}}^{(1)} = h_0^{\text{rf}}$ is larger than $H_{\text{eff},IS \times \text{rf}}^{(2)}$, it truncates this second-order Hamiltonian, and the ^1H - ^{35}Cl recoupling is governed by a Hamiltonian proportional to $h_0^{\text{rf}}S_z$, which converts S_x into ^1H - ^{35}Cl multiple-quantum coherences with 1Q-CT, 1Q-ST, 2Q-ST, and 3Q of ^{35}Cl isotope. In the case of a centerband irradiation, $H_{\text{eff},IS \times \text{rf}}^{(2)}$ is orthogonal to h_0^{rf} and the T-HMQC signal is null. When irradiating the midpoint between two consecutive spinning sidebands, the third-order effective Hamiltonian between two rf Hamiltonians and the ^1H - ^{35}Cl dipolar interaction in the form of Eq. (S2) can transform S_x into ^1H - ^{35}Cl multiple-quantum coherences involving 2Q-ST of ^{35}Cl isotope. Furthermore, the fourth-order effective Hamiltonian between three rf Hamiltonians and the ^1H - ^{35}Cl dipolar interaction (not shown) can convert S_x into ^1H - ^{35}Cl coherences with 1Q-CT, 1Q-ST, and 3Q for $\nu_{\text{off}} = (n \pm 1/3)\nu_R$.

E. Expression of the T-HMQC signal

For a ^1H - $\{I\}$ T-HMQC sequence, the phase cycling selects during t_1 . The coherence order of spin I , q_I , and the NMR signal is proportional to

$$\sum_{l,q_I} \langle (S_x | U_{\text{mix}} T_{l,q_I}^I U_{\text{mix}}^{-1}) (T_{l,q_I}^I | U_{t_1} T_{l,q_I}^I U_{t_1}^{-1}) (T_{l,q_I}^I | U_{\text{mix}} S_x U_{\text{mix}}^{-1}) \rangle, \quad (30)$$

where the angular bracket denotes the powder average and the scalar product in the operator space is defined by $(A|B) = \text{Tr}\{A^\dagger B\}$, with A^\dagger being the Hermitian adjoint of A . U_{mix} denotes the propagators for the two identical TRAPDOR pulses, which are equal when τ_{mix} and t_1 are multiples of T_R . In this case, when neglecting the third-order Hamiltonians, U_{mix} is equal to

$$U_{\text{mix}} = \exp \left[-i \left(H_{\text{eff},\text{rf} \times \text{rf}}^{(2),h_0} + H_{\text{eff},IS \times \text{rf}}^{(2),h_0} \right) \tau_{\text{mix}} \right], \quad (31)$$

where $H_{\text{eff},\text{rf}/IS \times \text{rf}}^{(2),h_0}$ are the projections of $H_{\text{eff},\text{rf}/IS \times \text{rf}}^{(2)}$ onto h_0^{rf} [Eq. (18)],

$$H_{\text{eff},\text{rf}/IS \times \text{rf}}^{(2),h_0} = \frac{\text{Tr} \left(h_0^{\text{rf},\dagger} H_{\text{eff},\text{rf}/IS \times \text{rf}}^{(2)} \right)}{\text{Tr} \left(h_0^{\text{rf},\dagger} h_0 \right)} h_0^{\text{rf}}. \quad (32)$$

In Eq. (30), U_{t_1} denotes the propagator for the t_1 evolution under the isotropic chemical and quadrupolar induced shifts, and T_{l,q_I}^I denotes the irreducible tensor operator of spin I , with rank $0 \leq l \leq 2I$ and coherence order $-l \leq q_I \leq +l$.⁸¹ The t_1 rotor-synchronization also ensures the absence of evolution under CSA, dipolar, and H_{Q1} interactions of I spin, and the evolution of the T_{l,q_I}^I operator during t_1 can be written as

$$(T_{l,q_I}^I | U_{t_1} T_{l,q_I}^I U_{t_1}^{-1}) = \exp(-iq_I \Omega_I^0 t_1), \quad (33)$$

where Ω_I^0 denotes the angular frequency corresponding to the isotropic shift. By substituting Eq. (33) into Eq. (30) and using the complex conjugation property of the scalar product and the invariance of the trace under cyclic permutation, Eq. (30) simplifies into

$$\sum_{l,q_I} \exp(-iq_I \Omega_I^0 t_1) \left| (T_{l,q_I}^I | U_{\text{mix}} S_x U_{\text{mix}}^{-1}) \right|^2. \quad (34)$$

As the last term of this equation is a real number, the coherence transfer during the T-HMQC sequence only modulates the amplitude of the signal, not its phase. Globally, this is due to the fact this scheme uses two identical long TRAPDOR pulses on the quadrupolar channel, symmetrical with respect to the refocusing π -pulse on the ^1H channel. This symmetry allows canceling the dephasings

under anisotropic interaction, hence increasing the sensitivity of the method. This feature contrasts with the conventional TRAP-DOR experiment,^{52–54} where only one long pulse is sent on the quadrupolar channel. In this case, the dephasings under anisotropic interaction are not refocused.

III. NUMERICAL SIMULATIONS

A. Simulation parameters

All numerical simulations of the $^1\text{H}\{-I\}$ T-HMQC sequence were performed using the SIMPSON software for an isolated $^1\text{H}\{-I\}$ pair without ^1H CSA.⁸² The powder average was calculated using 232 $\{\alpha_{\text{MR}}, \beta_{\text{MR}}\}$ pairs and 74 γ_{MR} Euler angles to relate the molecular and rotor frames in the case of $I = ^{195}\text{Pt}$, whereas we employed only 168 $\{\alpha_{\text{MR}}, \beta_{\text{MR}}\}$ pairs and 11 γ_{MR} angles for $I = ^{14}\text{N}$ and ^{35}Cl . The REPULSION algorithm was employed to select the $\{\alpha_{\text{MR}}, \beta_{\text{MR}}\}$ pairs,⁸³ whereas the γ_{MR} angles were regularly stepped between 0° and 360° .

For $I = ^{195}\text{Pt}$, the dipolar coupling was equal to $|b_{\text{H}\{-^{195}\text{Pt}\}}|/(2\pi) = 2$ kHz, whereas the ^{195}Pt CSA ranged from $\delta_{\text{aniso}}^{195\text{Pt}} \omega_{195\text{Pt}}^0 = 0.3$ MHz and η_{CSA} was equal to 0 or 1. For $I = ^{14}\text{N}$, the dipolar coupling was

equal to $|b_{\text{H}\{-^{14}\text{N}\}}|/(2\pi) = 1, 2,$ or 8 kHz, whereas the $\{C_Q; \eta_Q\}$ values were equal to $\{1.18 \text{ MHz}; 0.50\}$ or $\{3.21 \text{ MHz}; 0.32\}$, corresponding to the quadrupolar parameters of ^{14}N nuclei in glycine⁸⁴ or N-acetyl-L-valine (NAV).⁸⁵ For $I = ^{35}\text{Cl}$, the dipolar coupling was equal to $|b_{\text{H}\{-^{35}\text{Cl}\}}|/(2\pi) = 580$ Hz, whereas $C_Q = 1.95$ MHz and $\eta_Q = 0.66$, corresponding to the quadrupolar parameters of ^{35}Cl nuclei in L-histidine HCl.⁶¹

The static magnetic field was equal to $B_0 = 18.8$ T and the MAS frequency to 25 or 62.5 kHz. For all 1D simulations (Figs. 2–11 and Figs. S1–S3), the t_1 period was null, i.e., there was no window delay between the pulses on the I channel in order to avoid the evolution under the isotropic shift of I nuclei. The defocusing and refocusing periods were equal to an integer number of rotor-periods: $\tau_{\text{mix}} = mT_R$. The pulses on the ^1H channel were simulated as ideal Dirac ones. The long rectangular pulses on the I channel were applied on-resonance with the centerband for $I = ^{195}\text{Pt}$ and with the first spinning sideband for $I = ^{14}\text{N}$ and ^{35}Cl , except in Figs. 2, 5, 8, and 11, where we optimized the frequency offset, ν_{off} , which is defined as the difference between the carrier frequency and the sum of the isotropic chemical shift and the QIS. The transfer efficiency of the T-HMQC sequence was normalized with respect to

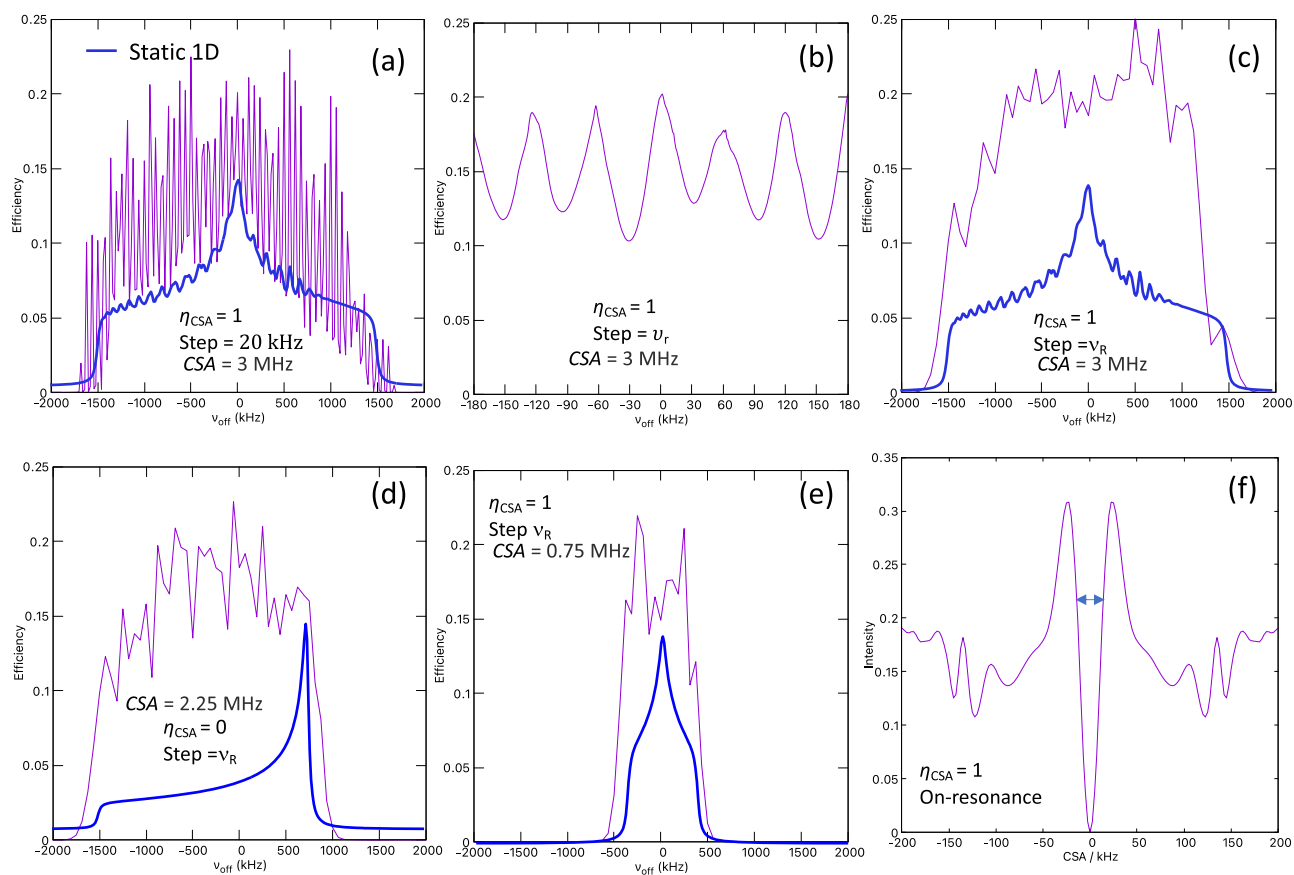


FIG. 2. Simulated efficiency of the $^1\text{H}\{-^{195}\text{Pt}\}$ T-HMQC sequence as a function of (a)–(e) offset and (f) CSA with $\nu_R = 62.5$ kHz, $\nu_1 = 50$ kHz, and $\tau_{\text{mix}} = 2$ ms. The panels (a) and (c)–(e) also display the 1D ^{195}Pt static spectra. Other simulation parameters are indicated in the panels.

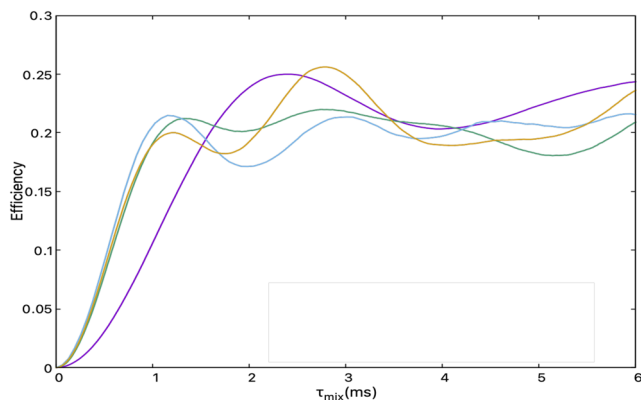


FIG. 3. Simulated build-up curves of the $^1\text{H}\{-^{195}\text{Pt}\}$ T-HMQC sequence with $\eta_{\text{CSA}} = 1$ and $\{\text{CSA (MHz)}, \nu_{\text{R}} \text{ (kHz)}, \nu_1 \text{ (kHz)}, \alpha\} = \{3, 62.5, 50, 0.013\}$ (purple), $\{3, 62.5, 100, 0.053\}$ (green), $\{3, 15.625, 50, 0.053\}$ (blue), and $\{0.75, 62.5, 50, 0.053\}$ (yellow). The adiabaticity parameter α is calculated with Eqs. (13) and (16).

that of a spin echo made of ideal Dirac pulses applied to the ^1H channel.

B. $^1\text{H}\{-^{195}\text{Pt}\}$ T-HMQC

Figures 2(a)–2(e) show the simulated efficiency of the $^1\text{H}\{-^{195}\text{Pt}\}$ T-HMQC sequence vs the ^{195}Pt offset for a $^1\text{H}\{-^{195}\text{Pt}\}$ spin

pair. These simulations demonstrate that the T-HMQC sequence can be applied for the indirect detection of ^{195}Pt nuclei, and more generally of any spin-1/2 isotope, subject to large shielding. For CSA ranging from ~ 50 –2000 kHz, the optimal transfer efficiency reaches $\sim 20\%$, instead of 50% for the $^1\text{H}\{-^{195}\text{Pt}\}$ D-HMQC sequence employing an rf-field larger than the CSA.⁷² The transfer efficiency of T-HMQC is maximal when irradiating one of the ^{195}Pt spinning sidebands [Fig. 2(b)], and contrary to ^{14}N and ^{35}Cl quadrupolar nuclei (see below), there is no drop in efficiency when irradiating the centerband. As seen in Eq. (11), the $^1\text{H}\{-^{195}\text{Pt}\}$ T-HMQC efficiency depends on the amplitudes of the $A_{n\pm p}$ terms, with $p = \pm 1$ and ± 2 , where n denotes the order of the irradiated spinning sideband and hence is determined by the envelope of the spinning sideband manifold. For instance, the transfer efficiency profile is symmetric with respect to the centerband for $\eta_{\text{CSA}} = 1$ [Figs. 2(a), 2(c), and 2(e)] and asymmetric otherwise [Fig. 2(d)]. Its excitation bandwidth is comparable to the full width of the static powder pattern [Eq. (13)]: $\text{CSA} = \delta_{\text{aniso}}^I \omega_I^0 (3 + \eta_{\text{CSA}})/2 \approx 3, 2.25$, and 0.75 MHz for $\{\delta_{\text{aniso}}^I \omega_I^0 \text{ (MHz)}, \eta_{\text{CSA}}\} = \{1.5, 1\}$, $\{1.5, 0\}$ and $\{0.375, 1\}$, as shown in Figs. 2(c)–2(e), respectively. As seen in Fig. 2(f), the T-HMQC efficiency cancels out for vanishing CSA. In that case, the theoretical treatment given in Sec. II B is not valid and the rf irradiation on the ^{195}Pt channel does not recouple the $^1\text{H}\{-^{195}\text{Pt}\}$ dipolar interaction.

Figure 3 displays the $^1\text{H}\{-^{195}\text{Pt}\}$ T-HMQC build-up curves simulated for different values of CSA, ν_{R} , and ν_1 parameters. These simulations confirm the validity of Eqs. (15) and (16), since build-up

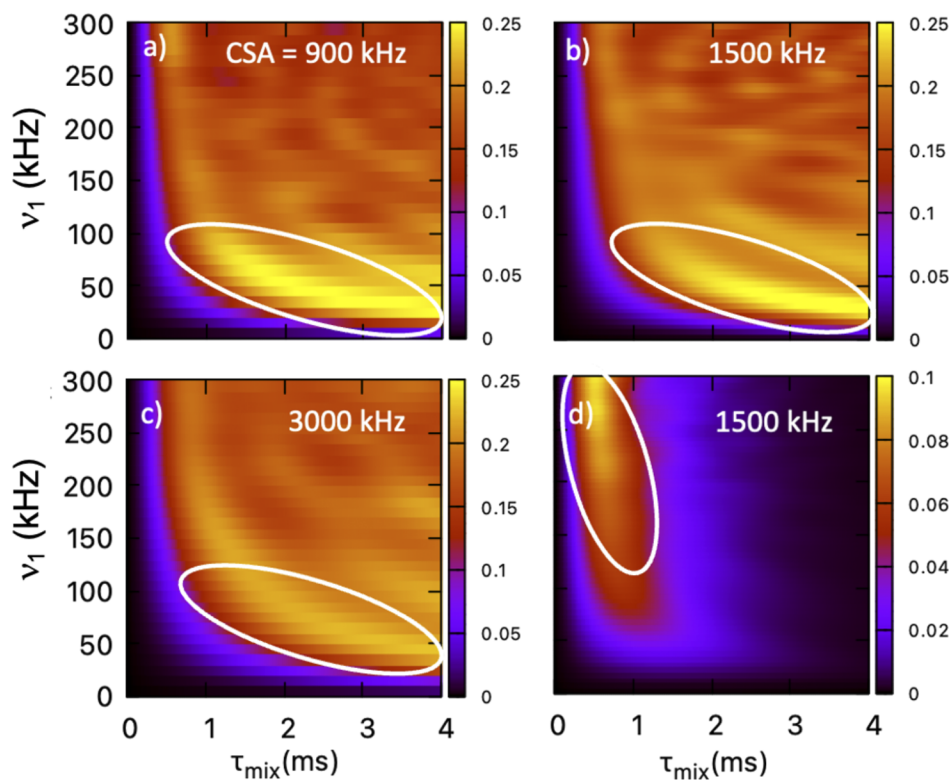


FIG. 4. Simulated on-resonance efficiency of the $^1\text{H}\{-^{195}\text{Pt}\}$ T-HMQC sequence vs ν_1 and τ_{mix} with $\nu_{\text{R}} = 62.5$ kHz and $\eta_{\text{CSA}} = 1$. The CSA values are indicated on the panels. In (d), the transfer efficiency shown in (b) has been multiplied by $\exp(-2\tau_{\text{mix}}/T_2')$ with $T_2' = 1.6$ ms in order to take into account the losses due to transverse relaxation during the recoupling periods. The efficiency scale of (d) differs from that of the other panels.

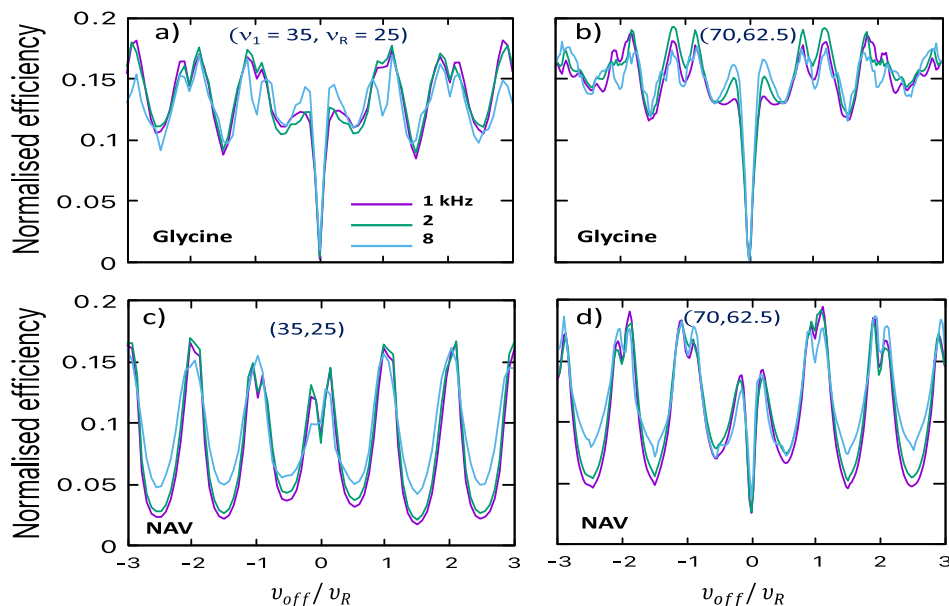


FIG. 5. Simulated $^1\text{H}\{-^{14}\text{N}^{1\text{Q}}\}$ T-HMQC efficiency vs v_{off} for $\tau_{\text{mix}} = 2$ ms, $|b_{1\text{H}-^{14}\text{N}}|/(2\pi) = 1, 2,$ and 8 kHz, and $(v_1, v_R) =$ (a) and (c) $(35, 25)$ and (b) and (d) $(70, 62.5)$ kHz.

curves with identical α values exhibit the same initial slope, whereas a fourfold reduction of the α parameter decreases the initial slope by a factor 2.

Figure 4 shows the efficiency of the $^1\text{H}\{-^{195}\text{Pt}\}$ T-HMQC sequence as a function of τ_{mix} and v_1 parameters. These simulations show that the optimal recoupling time is inversely proportional to v_1 in agreement with Eqs. (15) and (16), which predict that the strength of the recoupled dipolar interaction is proportional to v_1 . Furthermore, for a given τ_{mix} delay, the optimal v_1 increases with the CSA value in agreement with Eq. (16) [compare Figs. 4(a)–4(c)]. These

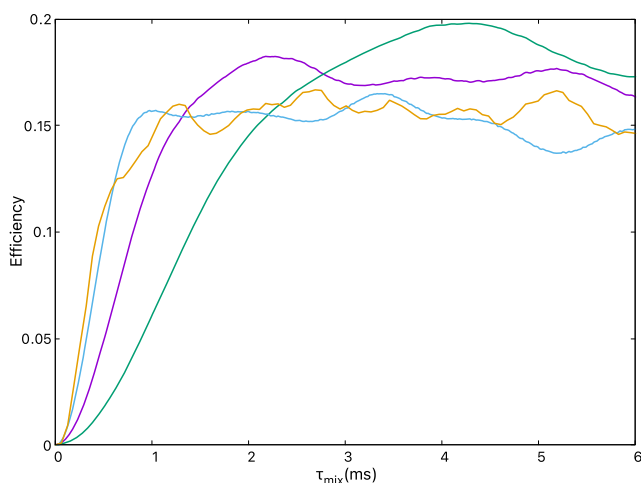


FIG. 6. Simulated $^1\text{H}\{-^{14}\text{N}^{1\text{Q}}\}$ T-HMQC build-up curves for $\{C_Q$ (MHz), v_R (kHz), v_1 (kHz), $\alpha\} = \{3.21, 62.5, 80, 0.021\}$ (purple), $\{3.21, 62.5, 40, 0.0053\}$ (green), $\{0.8, 62.5, 80, 0.085\}$ (blue), and $\{3.21, 15.625, 80, 0.085\}$ (yellow). The α parameter is calculated with Eq. (26) and $|b_{1\text{H}-^{14}\text{N}}|/(2\pi) = 2$ kHz and $v_{\text{off}} = v_R$.

simulations show that, in principle, an efficient recoupling can be achieved using long τ_{mix} delay and low v_1 amplitude, even in the case of large ^{195}Pt CSA. Nevertheless, in practice, the ^1H echo signal decays with the time constant, T_2' , of a few milliseconds because of residual $^1\text{H}\text{--}^1\text{H}$ dipolar interactions, which are not fully averaged out by MAS. As seen in Fig. 4(d), these losses can require the use of short τ_{mix} delay and hence high v_1 amplitude.

C. $^1\text{H}\{-^{14}\text{N}\}$ T-HMQC

The efficiency of the $^1\text{H}\{-^{14}\text{N}^{1\text{Q}}\}$ T-HMQC sequence as a function of offset is shown in Fig. 5. The offset profile does not strongly depend on the $^1\text{H}\text{--}^{14}\text{N}$ dipolar coupling. A major difference with respect to the simulated offset profile of the $^1\text{H}\{-^{195}\text{Pt}\}$ T-HMQC sequence shown in Fig. 2 is the trough for the on-resonance irradiation of the centerband, which has already been reported.⁵¹ This trough stems from the orthogonality of $H_{\text{eff},\text{IS}\times\text{rf}}^{(2)}$ and h_0^{rf} , which then fully decouples the $^1\text{H}\text{--}^{14}\text{N}$ dipolar interaction, as explained in Sec. II C. When irradiating the centerband, the transfer efficiency is higher in the case of NAV than that of glycine. This comes from the fact the anisotropic part of the $H_{\text{Q}2}$ interaction shifts $7.4 = (3.21/1.18)^2$ times more the frequency of the NAV centerband, depending on the crystallite orientation. As a result, the pulses on the ^{14}N channel do not irradiate the NAV centerband of all crystallites simultaneously. The maximum transfer efficiency is approximately equal to 20%, like for the ^{195}Pt nucleus. The efficiency also exhibits local minima for irradiations close to the spinning sidebands, in agreement with previously reported experimental results.⁵¹ These local minima stem from the creation of ^{14}N 2Q coherences by the third-order Hamiltonian of Eq. (S1), which is smaller than the second-order one. Therefore, its effects are more pronounced for large $^1\text{H}\text{--}^{14}\text{N}$ dipolar interactions (see Figs. 5 and 8).

The simulations of the $^1\text{H}\{-^{14}\text{N}^{1\text{Q}}\}$ T-HMQC build-up curves for different C_Q , v_R , and v_1 values, shown in Fig. 6, indicate that the

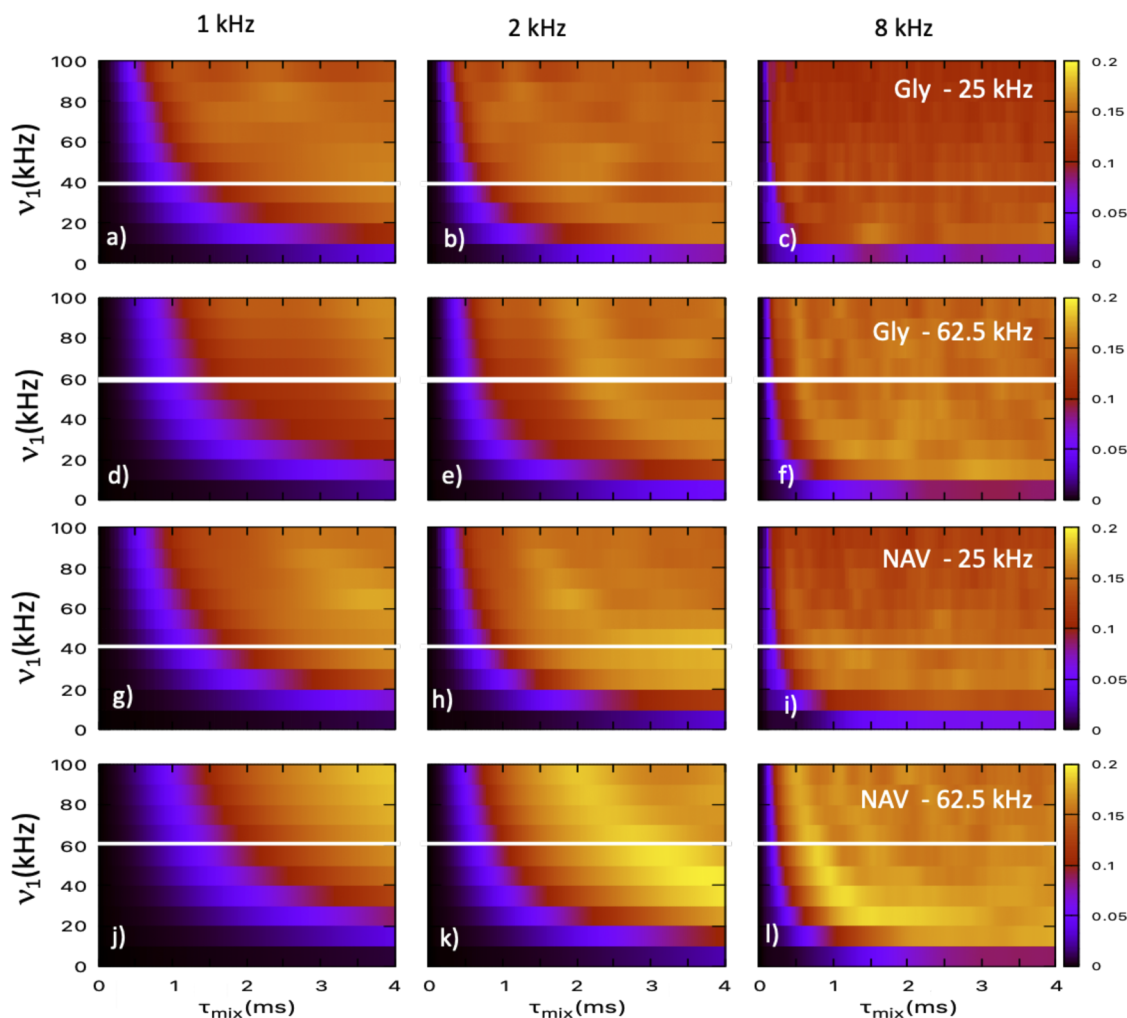


FIG. 7. Simulated $^1\text{H}\{-^{14}\text{N}^{1\text{Q}}\}$ T-HMQC efficiency vs τ_{mix} and ν_1 for (a)–(f) glycine and (g)–(l) NAV with $\nu_{\text{R}} = 25$ [(a)–(c) and (g)–(i)] or 62.5 [(d)–(f) and (j)–(l)] kHz. The $|b_{1\text{H}-^{14}\text{N}}|/(2\pi)$ value is indicated on the top line and $\nu_{\text{off}} = \nu_{\text{R}}$. The horizontal white lines show the rf field that can be accessed with 3.2 (40 kHz) or 1.3 mm (60 kHz) rotors at the ^{14}N Larmor frequency and $B_0 = 18.8$ T for $\nu_{\text{R}} = 25$ or 62.5 kHz, respectively.

initial slope increases slightly slower than $\sqrt{\alpha}$. This small discrepancy with Eq. (26) stems from the interference with the third-order effective Hamiltonian of Eq. (S1), which depletes the ^1H transverse magnetization by transforming it into ^{14}N 2Q coherences. The simulated build-up curves, shown in Fig. S1, also indicate that the initial slope of the build-up curves increases for increasing ν_1 amplitude and a lower C_{Q} constant.

The simulations of the $^1\text{H}\{-^{14}\text{N}^{1\text{Q}}\}$ T-HMQC efficiency as a function of τ_{mix} and ν_1 , shown in Fig. 7, also indicate that the optimal recoupling time is roughly inversely proportional to ν_1 in agreement with Eq. (26). Nevertheless, the short T_2' values of ^1H nuclei may prevent the use of a long τ_{mix} period and low ν_1 amplitude, as shown for the ^{195}Pt isotope. Furthermore, for a given τ_{mix} delay, large C_{Q} and ν_{R} values require the use of a higher rf-field, as predicted by Eq. (26). Nevertheless, at ultra-fast MAS, this requirement is offset

by the possibility of using longer τ_{mix} delays and hence smaller ν_1 values, since the T_2' constant of protons increases linearly with ν_{R} frequency.⁸⁶

The offset profiles of the $^1\text{H}\{-^{14}\text{N}^{2\text{Q}}\}$ T-HMQC sequence shown in Fig. 8 also exhibit a trough for the irradiation of the centerband, particularly for glycine with small $H_{\text{Q}2}$ broadening. Conversely, local minima around the spinning sidebands are not detected. In addition, these profiles exhibit additional maxima at the midpoints between the spinning sidebands, $\nu_{\text{off}} = (n + 1/2)\nu_{\text{R}}$, which stem from the third-order effective Hamiltonian [Eq. (S2)]. The buildup of the efficiency at these offsets is slower than for the irradiation at the spinning sidebands since the amplitude of the third-order term is proportional to α , instead of $\sqrt{\alpha} \geq \alpha$ for the second-order terms [compare Figs. S2(a) and S3].

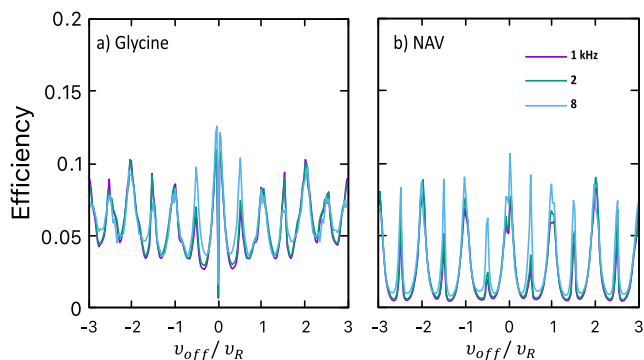


FIG. 8. Simulated $^1\text{H}\{-^{14}\text{N}^{2\text{Q}}\}$ T-HMQC efficiency vs v_{off} for glycine and NAV with $v_R = 62.5$ kHz, $v_1 = 70$ kHz, and $|b_{1\text{H}-^{14}\text{N}}|/(2\pi) = 1, 2$ or 8 kHz.

The initial slope of simulated build-up curves of the $^1\text{H}\{-^{14}\text{N}^{2\text{Q}}\}$ T-HMQC sequence (Fig. 9) also increases with α but with a slope slightly faster than $\sqrt{\alpha}$ owing to the contribution of the third-order Hamiltonian [Eq. (S1)] to the buildup of ^{14}N 2Q coherences. Additional simulated build-up curves shown in Fig. S2 also confirm that the initial slope increases with a higher rf-field and lower C_Q constant. The simulated efficiency of the $^1\text{H}\{-^{14}\text{N}^{2\text{Q}}\}$ T-HMQC sequence as a function of τ_{mix} delay and v_1 amplitude,

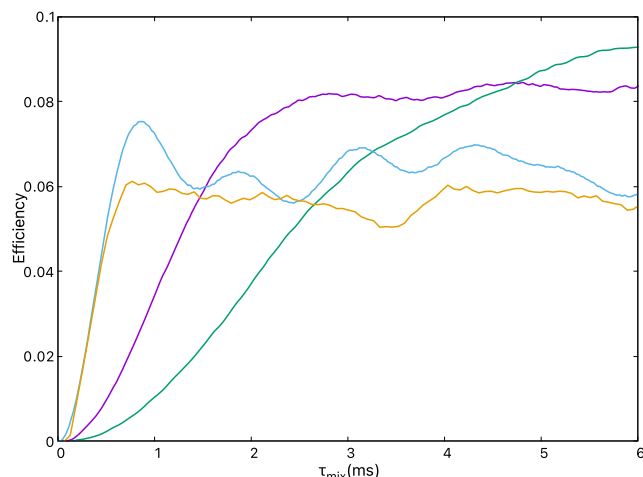


FIG. 9. Simulated $^1\text{H}\{-^{14}\text{N}^{2\text{Q}}\}$ T-HMQC build-up curves for $\{C_Q$ (MHz), v_R (kHz), v_1 (kHz), $\alpha\}$ = $\{3.21, 62.5, 80, 0.021\}$ (purple), $\{3.21, 62.5, 40, 0.053\}$ (green), $\{0.8, 62.5, 80, 0.085\}$ (blue), and $\{3.21, 15.625, 80, 0.085\}$ (yellow). The α parameter is calculated with Eq. (26), $|b_{1\text{H}-^{14}\text{N}}|/(2\pi) = 2$ kHz and $v_{\text{off}} = v_R$.

shown in Fig. 10, also indicates that the optimal τ_{mix} delay is inversely proportional to v_1 , whereas the optimal rf-field increases with C_Q and v_R values in agreement with Eq. (26). These simulations also indicate that the buildup of ^{14}N 2Q coherences is slightly

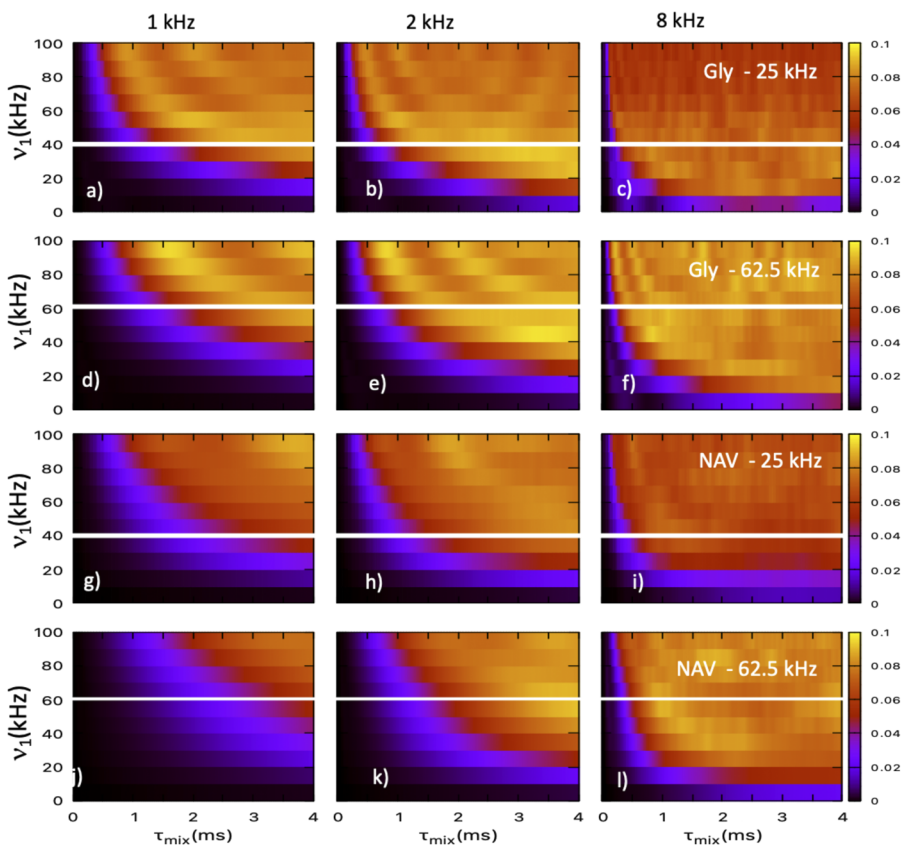


FIG. 10. Simulated $^1\text{H}\{-^{14}\text{N}^{2\text{Q}}\}$ T-HMQC efficiency vs τ_{mix} and v_1 for (a)–(f) glycine or (g)–(l) NAV with $v_R = 25$ [(a)–(c) and (g)–(i)] or 62.5 [(d)–(f) and (j)–(l)] kHz. The $|b_{1\text{H}-^{14}\text{N}}|/(2\pi)$ value is indicated on the first line and $v_{\text{off}} = v_R$. The horizontal white lines show the rf field that can be accessed with 3.2 (40 kHz) or 1.3 mm (60 kHz) rotors at the ^{14}N Larmor frequency and $B_0 = 18.8$ T for $v_R = 25$ or 62.5 kHz, respectively.

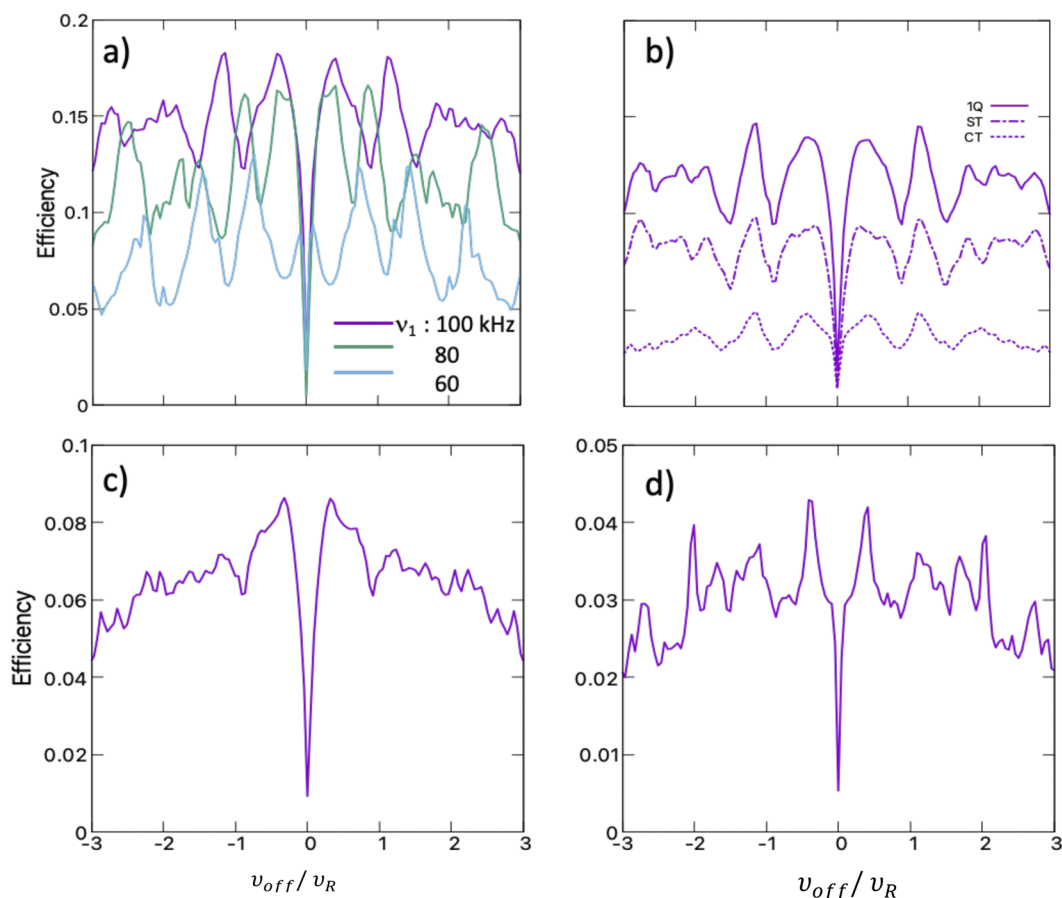


FIG. 11. Simulated $^1\text{H}\{-^{35}\text{Cl}\}$ T-HMQC efficiency vs the ν_{off}/ν_R ratio with the selection of ^{35}Cl coherences (a) 1Q + 3Q (two-step phase cycling with $\nu_1 = 60, 80$ or 100 kHz), (b) 1Q-(CT+ST), 1Q-CT and 1Q-ST, (c) 2Q-ST (four-step phase cycling), and (d) 3Q (six-step phase cycling). For the simulations of panels (b)–(d), $\nu_1 = 100$ kHz. The other simulation parameters are $B_0 = 18.8$ T, $\nu_R = 62.5$ kHz, $|b_{1\text{H}-^{35}\text{Cl}}|/(2\pi) = 0.58$, $C_Q = 1.95$ MHz, $\eta_Q = 0.66$, and $\tau_{\text{mix}} = 1.7$ ms.

slower than that of 1Q ones (compare Figs. S1 and S2) and the maximal transfer efficiency is 0.1, twice lower than that of the $^1\text{H}\{-^{14}\text{N}\}^1\text{Q}$ T-HMQC sequence.

D. $^1\text{H}\{-^{35}\text{Cl}\}$ T-HMQC

Figure 11 shows the efficiency vs offset of the $^1\text{H}\{-^{35}\text{Cl}\}$ T-HMQC sequence with two-, four-, and six-step phase cycling, which leads to the selection of 1Q + 3Q, 2Q, and 3Q coherences, respectively. For the sake of clarity, we will mention simultaneously these two aspects: the number of steps for the phase cycling and the corresponding selected coherence orders.

These offset profiles, like those of the $^1\text{H}\{-^{14}\text{N}\}$ T-HMQC experiments, exhibit a trough on-resonance owing to the orthogonality of $H_{\text{eff},\text{IS}\times\text{rf}}^{(2)}$ and h_0^{rf} in the case of centerband irradiation (Sec. II D), which decouples the $^1\text{H}\{-^{35}\text{Cl}\}$ dipolar interactions.

With a two-step phase cycling [1Q + 3Q: Fig. 11(a)], local maxima are observed with offsets depending on the rf-field applied to the ^{35}Cl channel. In particular, additional maxima are observed at

$\nu_{\text{off}} = \pm\nu_R/3$ for large rf-fields. They stem from the fourth-order effective Hamiltonian, which then contributes to the indirect detection of 1Q and 3Q ^{35}Cl coherences. These local maxima are also observed with a six-step phase cycling [3Q: Fig. 11(d)], whereas the offset profile with four-step phase cycling exhibit local maxima at $\nu_{\text{off}} = \pm\nu_R/2$ [2Q: Fig. 11(c)] since the third-order effective Hamiltonian contributes to the indirect detection of ^{35}Cl 2Q coherences. The transfer efficiencies of the $^1\text{H}\{-^{35}\text{Cl}\}$ T-HMQC sequence with two-, four-, and six-step phase cycling are approximately equal to 15%, 7%, and 3%, respectively. In the case of a two-step phase cycling, the 1Q-ST signal is two to three times more intense than that of 1Q-CT, which has an intensity comparable to that of 3Q.

IV. EXPERIMENTAL DEMONSTRATIONS

A. Samples and experimental conditions

Cis-platin, trans-platin, and L-histidine HCl-H₂O (referred to as “histidine” hereafter) were purchased from Merck. An equimolar mechanical mixture of cis- and trans-platin was prepared and packed into a 1.3 mm rotor, which was stored in the air during three

TABLE I. Experimental parameters (N_1 , τ_{RD} , NS , ν_R , and SW_1) of the $^1\text{H}\{-^{195}\text{Pt}\}$ T-HMQC 2D spectra along with the intensity of the cross-peak between $\delta_{^1\text{H}} = 4$ ppm and $\delta_{^{195}\text{Pt}} = -1795$ ppm and the root-mean-square (rms) amplitude of the noise.

Figures	N_1	τ_{RD} (s)	NS	ν_R (kHz)	SW_1 (kHz)	T_{exp} (min)	Intensity ^a	Noise ^b	Intensity/Noise
12(a)	60	20	16	64	64	322	1	1	1
12(b)	60	1	288	64	64	324	1.5	4	0.375
14(a)	240	10	8	64	256	321	0.66	0.7	0.94
14(b)	40 ^c	16	16	62	62	172	0.77	0.5	1.54

^aNormalized with respect to the cross-peak intensity in Fig. 12(a).^bMeasured in the F_1 slices devoid of the signal with $\delta_{^1\text{H}} = 32$ ppm and normalized with respect to that in Fig. 12(a).^cSelected using a bi-exponentially decaying sampling.⁸⁸

years.⁶² We chose this aged mixture in order to demonstrate the possibility to resolve using $^1\text{H}\{-^{195}\text{Pt}\}$ T-HMQC experiments the ^{195}Pt resonances of cis- and trans-platin as well as impurities. Owing to the robustness of the T-HMQC sequence to rf-field inhomogeneity, the sample volume in the rotor was not restricted with spacers.

All experiments were performed at $B_0 = 18.8$ T on a Bruker BioSpin Avance NEO spectrometer equipped with a double-resonance $^1\text{H}/X$ 1.3 mm MAS probe. The angle between the rotor axis and the B_0 field was carefully adjusted at the magic angle, whereas the MAS frequency was regulated using a MAS-III pneumatic unit with a standard deviation of 2.45 Hz (Fig. S4).

The ^1H rf-field for the $\pi/2$ and π pulses was set to $\nu_{^1\text{H}} = 208$ kHz. A pre-saturation consisting of five $\pi/2$ pulses was applied on the ^1H channel in order to use recycling delays shorter than five times the longitudinal relaxation time of protons $T_1(^1\text{H})$.

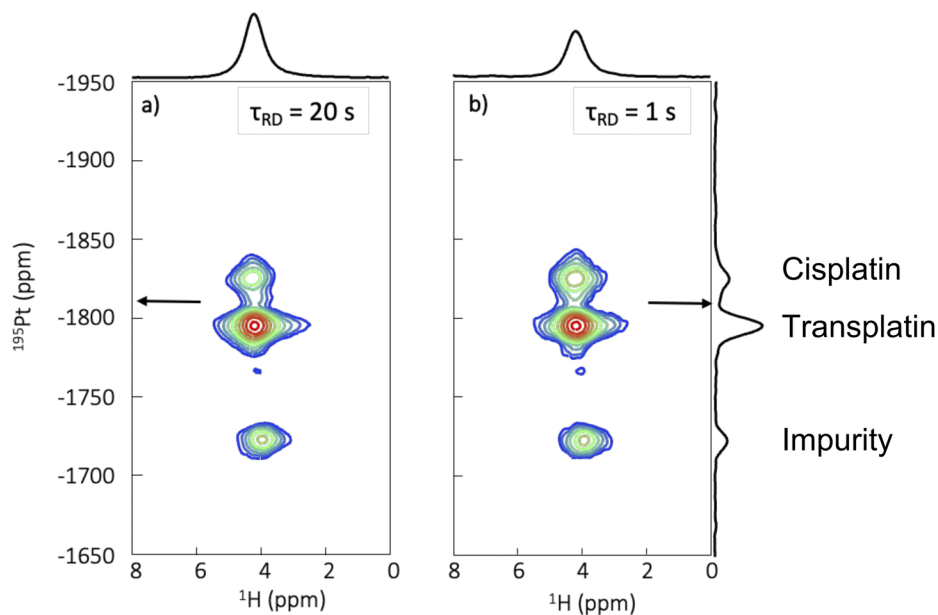
The ^1H isotropic chemical shifts were referenced to tetramethylsilane (TMS) using the signal of the CH_2 group of adamantane at 1.85 ppm as a secondary reference. The ^{195}Pt isotropic chemical shifts were indirectly referenced using the previously published relative NMR frequencies.⁸⁷

The aged mixture of cis- and trans-platin was spun at $\nu_R = 62$ and 64 kHz. The $^1\text{H}\{-^{195}\text{Pt}\}$ T-HMQC 2D spectra were recorded using two identical rectangular pulses with $\tau_{\text{mix}} = 516$ μs and $\nu_1 = 186$ kHz applied with a ^{195}Pt carrier frequency corresponding to a shift of $\delta_{\text{off}} = -1810$ or -1850 ppm. The other experimental parameters, including the number of t_1 increments, N_1 , the number of scans, NS , the recycling delay, τ_{RD} , the spectral width of the indirect dimension, SW_1 , and the total experimental time, T_{exp} , are listed in Table I.

The histidine sample was spun at $\nu_R = 50$ kHz. The $^1\text{H}\{-^{14}\text{N}\}$ T-HMQC spectra result from the averaging of $NS = 8$ transients for each of $N_1 = 128$ t_1 increments in the case of 2D spectra, with $SW_1 = \nu_R = \nu_1 = 50$ kHz, $\tau_{RD} = 1$ s and $\tau_{\text{mix}} = 540$ μs . The $^1\text{H}\{-^{35}\text{Cl}\}$ T-HMQC spectra result from averaging of $NS = 128$ transients for each t_1 increment with $SW_1 = \nu_R = \nu_1 = 50$ kHz and $\tau_{RD} = 1$ s.

B. $^1\text{H}\{-^{195}\text{Pt}\}$ T-HMQC

The $^1\text{H}\{-^{195}\text{Pt}\}$ T-HMQC experiment was tested on a mixture of cis- and trans-platin for which we recorded three years ago the

**FIG. 12.** $^1\text{H}\{-^{195}\text{Pt}\}$ T-HMQC 2D spectra of an aged mixture of cis- and trans-platin recorded at 18.8 T with $\nu_R = 64$ kHz, $\delta_{\text{off}} = -1810$ ppm (indicated with arrows), $SW_1 = \nu_R$, and $\tau_{RD} =$ (a) 20 or (b) 1 s.

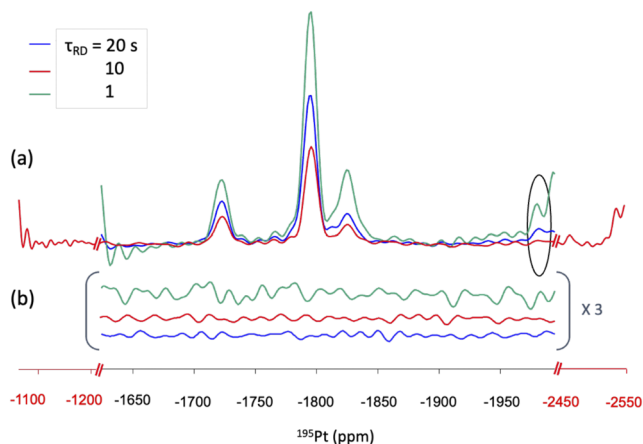


FIG. 13. 1D F_1 slices at $\delta_{1H} = 4$ (a) or 32 (b) ppm of the 2D $^1\text{H}\{-^{195}\text{Pt}\}$ T-HMQC spectra shown in Figs. 12 and 14 of an aged mixture of cis- and trans-platin recorded at 18.8 T with $\nu_R = 64$ kHz and $\delta_{\text{off}} = -1810$ ppm. The thermal noise has been scaled up by a factor of three in (b). The red slice in (a) is extracted from the 2D spectrum of Fig. 14(a) with $SW_1 = 4\nu_R$, and hence, additional regions corresponding to the edges of the spectra are also displayed to show the axial peaks. The oval indicates the region containing the impurity signal at -1990 ppm.

$^1\text{H}\{-^{195}\text{Pt}\}$ D-HMQC spectra.⁶⁸ In these square planar complexes, the ^{195}Pt nuclei are subject to a CSA ≈ 1.5 MHz at 18.8 T and a dipolar coupling $|b_{1\text{H}-^{195}\text{Pt}}|/(2\pi) = 2$ kHz.^{59,89}

The carrier frequency on the ^{195}Pt channel was applied at a frequency close to the centerband of the cis-platin and the first spinning

TABLE II. Shifts of ^{195}Pt resonances along the F_1 dimension of the $^1\text{H}\{-^{195}\text{Pt}\}$ T-HMQC 2D spectra of an aged mixture of cis- and trans-platin acquired at $\nu_R = 62$ and 64 kHz along with the δ_{iso} values calculated with Eq. (35).

Species	δ (64 kHz) (ppm)	δ (62 kHz) (ppm)	δ_{iso} (ppm)
Impurity-1	-1723	-1735	-2095
Trans-platin	-1795	-1807	-2167
Cis-platin	-1825	-1825	-1825
Impurity-2	-1990	-1990	-1990

sideband of trans-platin since according to simulations of Fig. 2, these conditions are expected to result in a maximal efficiency. We optimized both the τ_{mix} and ν_1 parameters (Fig. S5). As the T_2' values of cis- and trans-platin are equal to 1.6 ms, recoupling conditions corresponding to long recoupling time and low rf-power, such as $\tau_{\text{mix}} \approx 3$ ms and $\nu_1 \approx 50$ kHz, yielded a poor efficiency, as predicted by simulations of Fig. 4(d), and we had to use a short recoupling time and hence a high rf-power. The $^1\text{H}\{-^{195}\text{Pt}\}$ T-HMQC 2D spectra of Figs. 12 and 14 were recorded using $\tau_{\text{mix}} = 516 \mu\text{s}$ and $\nu_1 = 186$ kHz.

The $T_1(^1\text{H})$ constants of cis- and trans-platin are equal to 12 and 17 s, respectively.⁵⁹ We recorded the $^1\text{H}\{-^{195}\text{Pt}\}$ T-HMQC 2D spectrum with $SW_1 = \nu_R$ and $\tau_{\text{RD}} = 20$ s corresponding to $1.2T_1(^1\text{H})$ for cis-platin [Fig. 12(a)]. This recycling delay is close to that yielding maximal sensitivity when the thermal noise is dominating.⁹⁰ We also recorded the same spectrum with $\tau_{\text{RD}} = 1$ s since $\tau_{\text{RD}} < T_1(^1\text{H})$ limits the t_1 -noise, which is proportional to the signal intensity [Fig. 12(b)].⁴¹ Nevertheless, the 2D

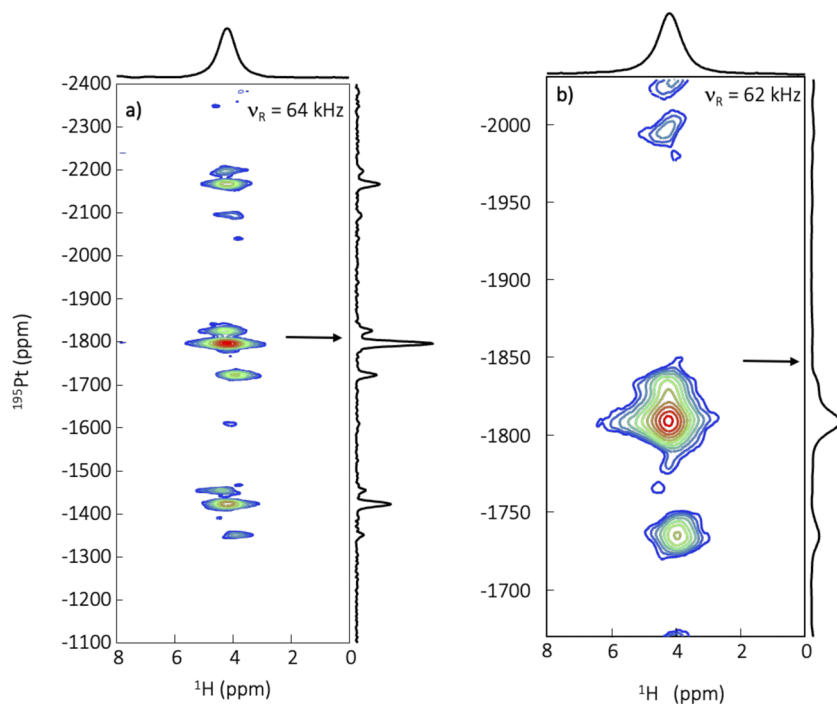


FIG. 14. $^1\text{H}\{-^{195}\text{Pt}\}$ T-HMQC 2D spectra of an aged mixture of trans- and cis-platin recorded at 18.8 T with (a) $\nu_R = 64$ kHz, $\delta_{\text{off}} = -1810$ ppm (indicated with arrow), $SW_1 = 4\nu_R$, and $\tau_{\text{RD}} = 10$ s and (b) $\nu_R = 62$ kHz, $\delta_{\text{off}} = -1850$ ppm (indicated with arrow), $SW_1 = \nu_R$, and $\tau_{\text{RD}} = 16$ s.

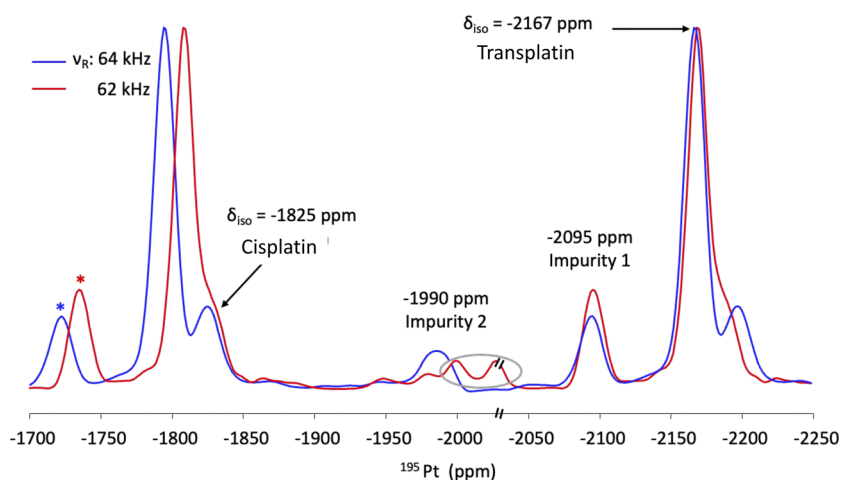


FIG. 15. 1D F_1 slices at $\delta_{1H} = 4$ ppm duplicated over $2\nu_R$ of the 2D $^1H\text{--}(^{195}Pt)$ T-HMQC spectra shown in Figs. 12(a) and 14(b) of an aged mixture of cis- and trans-platin recorded at 18.8 T with $\nu_R = 64$ and 62 kHz and $\delta_{off} = -1810$ or -1850 ppm, respectively. The centerbands are identified by their δ_{iso} values, and the symbol * denotes the spinning sidebands. The oval indicates the axial peak on the edge of the spectrum.

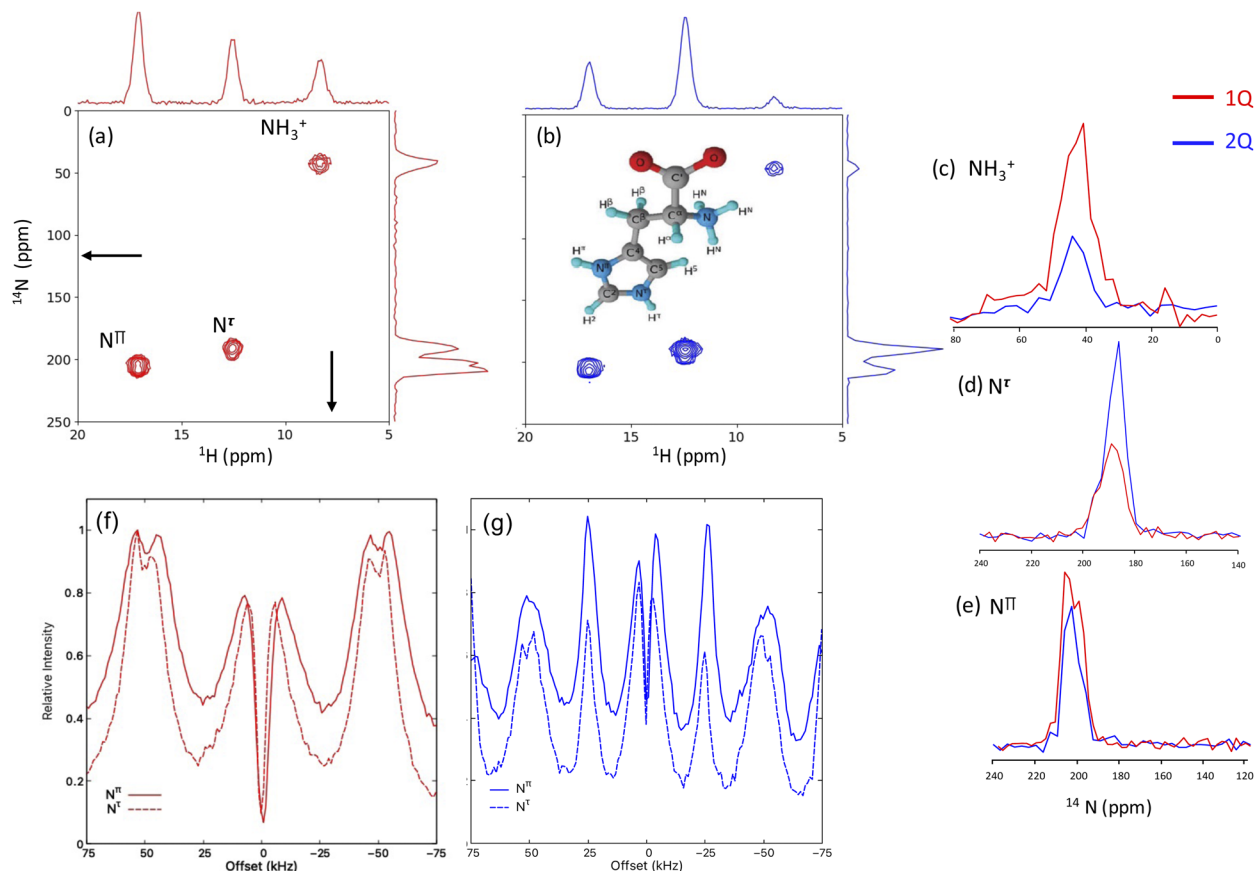


FIG. 16. (a) and (f) $^1H\text{--}(^{14}N^{1Q})$ and (b) and (g) $^1H\text{--}(^{14}N^{2Q})$ T-HMQC data on histidine at $B_0 = 18.8$ T with $\nu_R = 50$ kHz and $\tau_{mix} = 540$ μs . (a) $^1H\text{--}(^{14}N^{1Q})$ and (b) $^1H\text{--}(^{14}N^{2Q})$ 2D spectra along with their 1H and ^{14}N sum projections. The carrier frequencies are shown in (a) with arrows. (c)–(e) ^{14}N slices of these 2D spectra for (c) NH_3^+ , (d) N^ϵ , and (e) N^π sites without line-broadening. For the sake of comparison, the $^{14}N^{2Q}$ frequencies are divided by 2. (f) and (g) Efficiency of (f) $^1H\text{--}(^{14}N^{1Q})$ and (g) $^1H\text{--}(^{14}N^{2Q})$ T-HMQC 1D experiments vs ν_{off} for N^ϵ and N^π sites.

spectra of Fig. 12 do not exhibit significant t_1 -noise in agreement with the previously reported $^1\text{H}\{-^{14}\text{N}\}$ T-HMQC 2D spectra,⁵¹ and the largest signal-to-noise ratio (SNR) and sensitivity were obtained for $\tau_{\text{RD}} = 20$ s.

The cross-peaks detected on the 2D spectra of Fig. 12 demonstrate that T-HMQC can be used for the indirect detection of spin-1/2 nuclei subject to large CSA, such as ^{195}Pt . Three peaks are resolved at the shifts -1723 , -1795 , and -1825 ppm. Furthermore, as seen in Fig. 13, axial peaks, which do not evolve under ^{195}Pt isotropic chemical shifts, are detected at the edges of the T-HMQC 2D spectra. These axial peaks, which are rejected at the edges of the 2D spectra by the States-TPPI (time-proportional phase incrementation) procedure,⁹¹ stem from the evolution under the Bloch-Siegert shift [Eq. (9)]. Indeed, the amplitude of this term is constant, and as its phase does not depend of that of the rf pulse, these peaks cannot be eliminated by the phase cycling.

The isotropic chemical shifts of the different signals, δ_{iso} , were determined by recording two T-HMQC spectra at two slightly different MAS frequencies, $\nu_{\text{R},1}$ and $\nu_{\text{R},2}$,

$$\delta_{\text{iso}} = \delta(\nu_{\text{R},i}) - \frac{10^6 n \nu_{\text{R},i}}{\nu_0}, \quad (35)$$

where $\delta(\nu_{\text{R},i})$ is the shift measured at $\nu_{\text{R},i}$ and n is the order of the spinning sideband, which can be determined as

$$n = \nu_0 \frac{\delta(\nu_{\text{R},1}) - \delta(\nu_{\text{R},2})}{10^6 (\nu_{\text{R},1} - \nu_{\text{R},2})}. \quad (36)$$

The δ_{iso} values measured from the T-HMQC 2D spectra acquired at $\nu_{\text{R}} = 62$ and 64 kHz are listed in Table II. The shifts -1825 and -2167 ppm are assigned to cis- and trans-platin complexes, respectively.^{55,68,89} Additional ^{195}Pt resonances with $\delta_{\text{iso}} = -1990$ and -2095 ppm are detected. They are assigned to impurities formed during the aging of the mixture. The resonance with $\delta_{\text{iso}} = -1990$ ppm is better seen in the spectrum acquired at $\nu_{\text{R}} = 62$ kHz since it partly overlaps with the axial peak at $\nu_{\text{R}} = 64$ kHz [compare Figs. 13(a) and 14(b)]. As seen in Fig. 15, the signal with $\delta_{\text{iso}} = -2095$ ppm is more intense than that with $\delta_{\text{iso}} = -1990$ ppm. Therefore, these impurities with $\delta_{\text{iso}} = -1990$ and -2095 ppm could tentatively be assigned to mono-aquated cis- and trans-platin complexes $[\text{PtCl}(\text{NH}_3)_2(\text{H}_2\text{O})]^+$.⁹²

C. $^1\text{H}\{-^{14}\text{N}\}$ T-HMQC

Figures 16(a) and 16(b) show the $^1\text{H}\{-^{14}\text{N}^{1\text{Q}}\}$ and $^1\text{H}\{-^{14}\text{N}^{2\text{Q}}\}$ T-HMQC 2D spectra of histidine. Figures 16(c)–16(e) compare the ^{14}N slices of these 2D spectra for the three nitrogen sites, NH_3^+ , N^τ , and N^π , which are subject to similar quadrupole interactions,

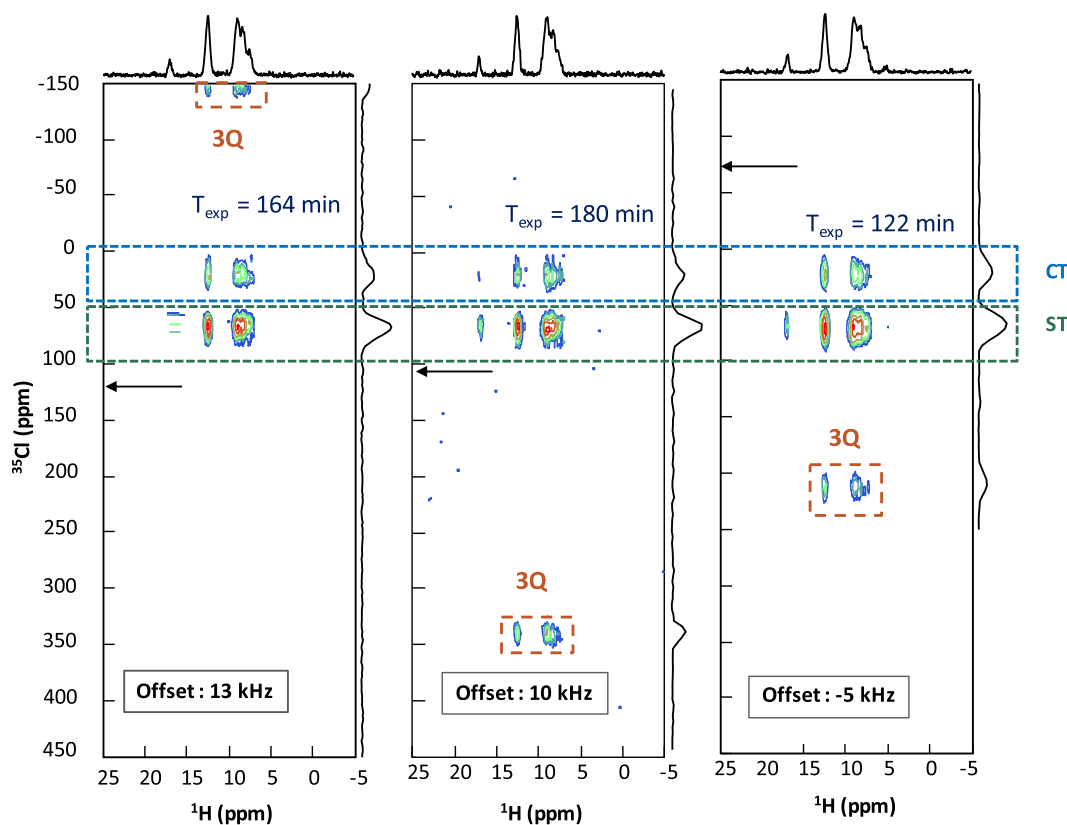


FIG. 17. $^1\text{H}\{-^{35}\text{Cl}^{1\text{Q}+3\text{Q}}\}$ T-HMQC 2D spectra of histidine at $B_0 = 18.8$ T with $\nu_{\text{R}} = 50$ kHz and different ^{35}Cl carrier frequencies indicated by arrows ($\nu_{\text{off}} = 13, 10$, and -5 kHz with $N_1 = 77, 84$, and 57 , respectively).

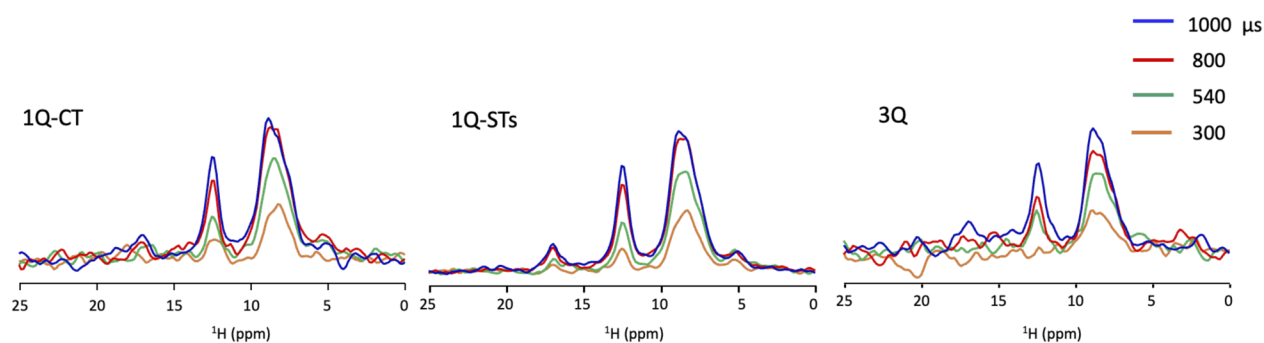


FIG. 18. $^1\text{H}\{-^{35}\text{Cl}\}^{1\text{Q}+3\text{Q}}$ T-HMQC spectra of histidine at $B_0 = 18.8$ T with $\nu_R = 50$ kHz and $\nu_{\text{off}} = -5$ kHz. For each detected coherence, we show five ^1H slices corresponding to $\tau_{\text{mix}} = 300, 500, 800,$ and 1000 μs (as indicated).

$\{C_Q$ (MHz), $\eta_Q\} = \{1.25, 0.35\}, \{1.29, 0.94\},$ and $\{1.56, 0.26\}$.⁹³ The $^{14}\text{N}^{2\text{Q}}$ frequencies were divided by a factor of two and no line broadening was applied to facilitate the comparison of the resolution with $^{14}\text{N}^{1\text{Q}}$. The $^{14}\text{N}^{2\text{Q}}$ resonances are slightly narrower than the $^{14}\text{N}^{1\text{Q}}$ ones despite the high stability of the MAS frequency and the careful setup of the magic angle. This result indicates that the $^1\text{H}\{-^{14}\text{N}^{2\text{Q}}\}$ T-HMQC 2D spectra benefit from a slightly improved resolution because they are not subject to H_{Q1} interaction.

The efficiency of the $^1\text{H}\{-^{14}\text{N}^{1\text{Q}}\}$ and $^1\text{H}\{-^{14}\text{N}^{2\text{Q}}\}$ T-HMQC experiments was optimized by adjusting τ_{mix} and ν_1 parameters, as shown in Fig. S6. The $^{14}\text{N}^{2\text{Q}}$ version requires a higher rf-field than the $^{14}\text{N}^{1\text{Q}}$ one. This difference could stem from the contribution of the third-order Hamiltonian to the creation of 2Q coherences. In practice, we used the highest rf-field on the ^{14}N channel compatible with the probe specifications. Under this condition, the experimental signal intensities of the $^1\text{H}\{-^{14}\text{N}^{1\text{Q}}\}$ and $^1\text{H}\{-^{14}\text{N}^{2\text{Q}}\}$ T-HMQC experiments are comparable [Figs. 16(c)–16(e)], whereas simulations predicted higher transfer efficiencies for the former technique. The decreased signal intensity of the $^1\text{H}\{-^{14}\text{N}^{1\text{Q}}\}$ T-HMQC experiment can stem from its higher sensitivity to instabilities of the MAS frequency and the magic angle.

The offset profiles of the $^1\text{H}\{-^{14}\text{N}^{1\text{Q}}\}$ and $^1\text{H}\{-^{14}\text{N}^{2\text{Q}}\}$ T-HMQC experiments shown in Figs. 16(f) and 16(g), respectively, agree with the simulated ones of Figs. 5 and 8. They exhibit a trough for the irradiation of the centerband. For the $^{14}\text{N}^{1\text{Q}}$ version, the maximal intensity is obtained when irradiating near the spinning sidebands. Nevertheless, local minima for the on-resonance irradiation of the spinning sidebands are detected since this condition favors the creation of ^{14}N 2Q coherences by the third-order Hamiltonian. In the case of the $^{14}\text{N}^{2\text{Q}}$ experiment, a maximal intensity is achieved at the frequencies of the spinning sidebands and their midpoints.

D. $^1\text{H}\{-^{35}\text{Cl}\}$ T-HMQC

Figure 17 displays the $^1\text{H}\{-^{35}\text{Cl}\}^{1\text{Q}+3\text{Q}}$ T-HMQC 2D spectra of histidine, which contains a single ^{35}Cl site with $C_Q = 1.95$ MHz and $\eta_Q = 0.66$.⁶¹ The two-step phase cycling of one of the

TRAPDOR pulse selects the 1Q-CT, 1Q-ST, and 3Q coherences during the t_1 period.⁶² These transitions can be distinguished by changing the offset since the dependence of the resonance frequency of 3Q coherences with the offset, ν_{off} , is fourfold larger than for the 1Q coherences. This “strange” effect comes from the States-TPPI acquisition used here with a phase shift of 90° . This corresponds to an effective rotation of $270^\circ = -90^\circ$ for the 3Q coherence in the rotating frame and hence to a negative frequency shift of $-\nu_{\text{off}}$. Therefore, the combined effects make the position of the 3Q coherence shifting by $4\nu_{\text{off}}$.

Figure 18 shows similar buildup for the three resonances with an optimal recoupling time $\tau_{\text{mix}} \approx 900$ μs . In agreement with the simulations, 1Q-CT and 3Q resonances exhibit similar intensities. Theoretically, these intensities should be twofold lower than that of 1Q-ST [Fig. 11(b)]. However, they all present similar experimental intensities because the intensity of the 1Q-ST strongly depends on the adjustment of the magic angle.

V. CONCLUSION

We have demonstrated for the first time the possibility to detect via protons the signal of spin-1/2 nuclei subject to large CSA using the T-HMQC sequence. We have shown that this experiment also allows the indirect observation of ^{14}N 2Q coherences, which is more robust than that of 1Q coherences, which are broadened by the first-order quadrupole interaction. In practice, the $^1\text{H}\{-^{14}\text{N}^{2\text{Q}}\}$ T-HMQC technique benefits from a better resolution than the $^{14}\text{N}^{1\text{Q}}$ variant, whereas both experiments offer similar sensitivities. We have also introduced effective Hamiltonians to describe the spin dynamics during the $^1\text{H}\{-I\}$ T-HMQC sequences with $I = 1/2, 1,$ and $3/2$. These Hamiltonians (i) explain the importance of the adiabaticity parameter for the TRAPDOR and T-HMQC experiments and (ii) highlight the contribution of terms with order higher than two, notably for the creation of multiple-quantum coherences. Using high MAS frequencies, ν_R , is beneficial for these $^1\text{H}\{-I\}$ T-HMQC experiments derived from the ^1H spin echo sequence. Indeed, on the one hand, the efficiency is inverse proportional to $\sqrt{\nu_R}$, but on the other hand, high MAS frequencies enhance the ^1H resolution and lengthen the T_2' value. Moreover, the small rotor diameters

associated with high MAS frequencies allow using larger rf-fields that increase the efficiency proportionally.

Actually, from the experiments presented in this article and from others not shown, we have always observed experimentally similar efficiencies with *D*- and T-HMQC experiments, whatever the MAS spinning speed: moderate or fast.

SUPPLEMENTARY MATERIAL

See the [supplementary material](#) for the third-order effective Hamiltonian for $I = 1$ [Eqs. (S1) and (S2)], simulated $^1\text{H}\text{-}\{^{14}\text{N}\}$ T-HMQC build-up curves, MAS frequency distribution, and experimental optimization of $^1\text{H}\text{-}\{^{195}\text{Pt}\}$ and $^1\text{H}\text{-}\{^{14}\text{N}\}$ T-HMQC 2D experiments.

ACKNOWLEDGMENTS

Chevreur Institute (Grant No. FR 2638), Ministère de l'Enseignement Supérieur, de la Recherche et de l'Innovation, Hauts-de-France Region, and FEDER are acknowledged for supporting and partially funding this work. Financial support from the IR-RMN-THC FR-3050 CNRS for conducting the research is gratefully acknowledged. O.L. and R.B. acknowledge financial support from Contract No. ANR-18-CE08-0015-01 (ThinGlass) and T-UEPEARL-20-005-LAFON-HAMDOUNA (NMR-MECA-DRUG). I.H. and Z.G. acknowledge support from the National Science Foundation through Grant No. NSF/DMR-1644779 and the State of Florida to the National High Magnetic Field Laboratory.

AUTHOR DECLARATIONS

Conflict of Interest

The authors declare no conflict of interest.

Author Contributions

All authors contributed equally to this work.

DATA AVAILABILITY

The data that support the findings of this study are available within the article and its [supplementary material](#).

REFERENCES

- B. Reif, S. E. Ashbrook, L. Emsley, and M. Hong, "Solid-state NMR spectroscopy," *Nat. Rev. Methods Primers* **1**, 2 (2021).
- R. W. Schurko, "Acquisition of wide-line solid-state NMR spectra of quadrupolar nuclei," in *Encyclopedia of Magnetic Resonance*, edited by R. K. Harris and R. Wasylishen (John Wiley, Chichester, 2011).
- R. W. Schurko, "Ultra-wide-line solid-state NMR spectroscopy," *Acc. Chem. Res.* **46**, 1985–1995 (2013).
- A. J. Pell, G. Pintacuda, and C. P. Grey, "Paramagnetic NMR in solution and the solid state," *Prog. Nucl. Magn. Reson. Spectrosc.* **111**, 1–271 (2019).
- S. E. Ashbrook and S. Seddon, "New methods and applications in solid-state NMR spectroscopy of quadrupolar nuclei," *J. Am. Chem. Soc.* **136**, 15440–15456 (2014).
- I. Hung, A. J. Rossini, and R. W. Schurko, "Application of the Carr–Purcell Meiboom–Gill pulse sequence for the acquisition of solid-state NMR spectra of spin-1/2 nuclei," *J. Phys. Chem. A* **108**, 7112–7120 (2004).
- R. Siegel, T. T. Nakashima, and R. E. Wasylishen, "Application of multiple-pulse experiments to characterize broad NMR chemical-shift powder patterns from spin-1/2 nuclei in the solid state," *J. Phys. Chem. B* **108**, 2218–2226 (2004).
- F. H. Larsen, H. J. Jakobsen, P. D. Ellis, and N. C. Nielsen, "Sensitivity-enhanced quadrupolar-echo NMR of half-integer quadrupolar nuclei. Magnitudes and relative orientation of chemical shielding and quadrupolar coupling tensors," *J. Phys. Chem. A* **101**, 8597–8606 (1997).
- K. J. Harris, A. Lupulescu, B. E. G. Lucier, L. Frydman, and R. W. Schurko, "Broadband adiabatic inversion pulses for cross polarization in wide-line solid-state NMR spectroscopy," *J. Magn. Reson.* **224**, 38–47 (2012).
- K. J. Harris, S. L. Veinberg, C. R. Mireault, A. Lupulescu, L. Frydman, and R. W. Schurko, "Rapid acquisition of ^{14}N solid-state NMR spectra with broadband cross polarization," *Chem. - Eur. J.* **19**, 16469–16475 (2013).
- T. Kobayashi, F. A. Perras, T. W. Goh, T. L. Metz, W. Huang, and M. Pruski, "DNP-enhanced ultrawide-line solid-state NMR spectroscopy: Studies of platinum in metal–organic frameworks," *J. Phys. Chem. Lett.* **7**, 2322–2327 (2016).
- D. A. Hirsh, A. J. Rossini, L. Emsley, and R. W. Schurko, " ^{35}Cl dynamic nuclear polarization solid-state NMR of active pharmaceutical ingredients," *Phys. Chem. Chem. Phys.* **18**, 25893–25904 (2016).
- I. Hung and R. W. Schurko, "Solid-state ^{91}Zr NMR of bis(cyclopentadienyl)dichlorozirconium(IV)," *J. Phys. Chem. B* **108**, 9060–9069 (2004).
- L. A. O'Dell, A. J. Rossini, and R. W. Schurko, "Acquisition of ultra-wide-line NMR spectra from quadrupolar nuclei by frequency stepped WURST–QCPMG," *Chem. Phys. Lett.* **468**, 330–335 (2009).
- L. A. O'Dell and R. W. Schurko, "Fast and simple acquisition of solid-state ^{14}N NMR spectra with signal enhancement via population transfer," *J. Am. Chem. Soc.* **131**, 6658–6659 (2009).
- A. W. MacGregor, L. A. O'Dell, and R. W. Schurko, "New methods for the acquisition of ultra-wide-line solid-state NMR spectra of spin-1/2 nuclides," *J. Magn. Reson.* **208**, 103–113 (2011).
- D. Massiot, I. Farnan, N. Gautier, D. Trumeau, A. Trokiner, and J. P. Coutures, " ^{71}Ga and ^{69}Ga nuclear magnetic resonance study of beta- Ga_2O_3 : Resolution of four- and six-fold coordinated Ga sites in static conditions," *Solid State Nucl. Magn. Reson.* **4**, 241–248 (1995).
- S. Cavadini, A. Lupulescu, S. Antonijevic, and G. Bodenhausen, "Nitrogen-14 NMR spectroscopy using residual dipolar splittings in solids," *J. Am. Chem. Soc.* **128**, 7706–7707 (2006).
- Z. Gan, "Measuring amide nitrogen quadrupolar coupling by high-resolution $^{14}\text{N}/^{13}\text{C}$ NMR correlation under magic-angle spinning," *J. Am. Chem. Soc.* **128**, 6040–6041 (2006).
- S. Cavadini, S. Antonijevic, A. Lupulescu, and G. Bodenhausen, "Indirect detection of nitrogen-14 in solids via protons by nuclear magnetic resonance spectroscopy," *J. Magn. Reson.* **182**, 168–172 (2006).
- J. P. Yesinowski and E. A. Hill, "Wide-line ^{14}N NMR in solids," in *Solid-State NMR Spectroscopy of Inorganic Materials* (American Chemical Society, 1999), pp. 358–376.
- S. Antonijevic and N. Halpern-Manners, "Probing amide bond nitrogens in solids using ^{14}N NMR spectroscopy," *Solid State Nucl. Magn. Reson.* **33**, 82–87 (2008).
- S. Cavadini, A. Abraham, and G. Bodenhausen, "Coherence transfer between spy nuclei and nitrogen-14 in solids," *J. Magn. Reson.* **190**, 160–164 (2008).
- Z. Gan, J. P. Amoureux, and J. Trébosc, "Proton-detected ^{14}N MAS NMR using homonuclear decoupled rotary resonance," *Chem. Phys. Lett.* **435**, 163–169 (2007).
- S. Cavadini, A. Abraham, and G. Bodenhausen, "Proton-detected nitrogen-14 NMR by recoupling of heteronuclear dipolar interactions using symmetry-based sequences," *Chem. Phys. Lett.* **445**, 1–5 (2007).
- A. Brinkmann and A. P. M. Kentgens, "Proton-selective $^{17}\text{O}\text{-}^1\text{H}$ distance measurements in fast magic-angle-spinning solid-state NMR spectroscopy for the determination of hydrogen bond lengths," *J. Am. Chem. Soc.* **128**, 14758–14759 (2006).
- O. Lafon, Q. Wang, B. Hu, F. Vasconcelos, J. Trébosc, S. Cristol, F. Deng, and J.-P. Amoureux, "Indirect detection via spin-1/2 nuclei in solid state NMR spectroscopy: Application to the observation of proximities between protons and quadrupolar nuclei," *J. Phys. Chem. A* **113**, 12864–12878 (2009).

- ²⁸M. Shen, J. Trébosc, O. Lafon, Z. Gan, F. Pourpoint, B. Hu, Q. Chen, and J.-P. Amoureux, "Solid-state NMR indirect detection of nuclei experiencing large anisotropic interactions using spinning sideband-selective pulses," *Solid State Nucl. Magn. Reson.* **72**, 104–117 (2015).
- ²⁹M. Shen, J. Trébosc, L. A. O'Dell, O. Lafon, F. Pourpoint, B. Hu, Q. Chen, and J.-P. Amoureux, "Comparison of various NMR methods for the indirect detection of nitrogen-14 nuclei via protons in solids," *J. Magn. Reson.* **258**, 86–95 (2015).
- ³⁰A. G. M. Rankin, J. Trébosc, P. Paluch, O. Lafon, and J.-P. Amoureux, "Evaluation of excitation schemes for indirect detection of ^{14}N via solid-state HMQC NMR experiments," *J. Magn. Reson.* **303**, 28–41 (2019).
- ³¹V. Vitzthum, M. A. Caporini, S. Ulzega, and G. Bodenhausen, "Broadband excitation and indirect detection of nitrogen-14 in rotating solids using Delays Alternating with Nutation (DANTE)," *J. Magn. Reson.* **212**, 234–239 (2011).
- ³²Y. Li, J. Trébosc, B. Hu, M. Shen, J.-P. Amoureux, and O. Lafon, "Indirect detection of broad spectra in solid-state NMR using interleaved DANTE trains," *J. Magn. Reson.* **294**, 101–114 (2018).
- ³³A. J. Pell, K. J. Sanders, S. Wegner, G. Pintacuda, and C. P. Grey, "Low-power broadband solid-state MAS NMR of ^{14}N ," *J. Chem. Phys.* **146**, 194202 (2017).
- ³⁴R. Aleksis and A. J. Pell, "Low-power synchronous helical pulse sequences for large anisotropic interactions in MAS NMR: Double-quantum excitation of ^{14}N ," *J. Chem. Phys.* **153**, 244202 (2020).
- ³⁵Y. Nishiyama, M. Malon, Z. Gan, Y. Endo, and T. Nemoto, "Proton–nitrogen-14 overtone two-dimensional correlation NMR spectroscopy of solid-sample at very fast magic angle sample spinning," *J. Magn. Reson.* **230**, 160–164 (2013).
- ³⁶L. A. O'Dell, R. He, and J. Pandohee, "Identifying H–N proximities in solid-state NMR using ^{14}N overtone irradiation under fast MAS," *CrytEngComm* **15**, 8657–8667 (2013).
- ³⁷M. Shen, Q. Chen, J.-P. Amoureux, and B. Hu, "Broad-band excitation in indirectly detected ^{14}N overtone spectroscopy with composite pulses," *Solid State Nucl. Magn. Reson.* **78**, 5–8 (2016).
- ³⁸R. Tycko and S. J. Opella, "High-resolution nitrogen-14 overtone spectroscopy: An approach to natural abundance nitrogen NMR of oriented and polycrystalline systems," *J. Am. Chem. Soc.* **108**, 3531–3532 (1986).
- ³⁹M. Shen, S. Wegner, J. Trébosc, B. Hu, O. Lafon, and J. P. Amoureux, "Minimizing the t_1 -noise when using an indirect ^1H high-resolution detection of unlabeled samples," *Solid State Nucl. Magn. Reson.* **87**, 111–116 (2017).
- ⁴⁰A. Venkatesh, X. Luan, F. A. Perras, I. Hung, W. Huang, and A. J. Rossini, " t_1 -noise eliminated dipolar heteronuclear multiple-quantum coherence solid-state NMR spectroscopy," *Phys. Chem. Chem. Phys.* **22**, 20815–20828 (2020).
- ⁴¹F. A. Perras and M. Pruski, "Reducing t_1 noise through rapid scanning," *J. Magn. Reson.* **298**, 31–34 (2019).
- ⁴²Z. Gan, "Measuring multiple carbon–nitrogen distances in natural abundant solids using R-RESPDOR NMR," *Chem. Commun.* **2006**, 4712–4714.
- ⁴³L. Chen, Q. Wang, B. Hu, O. Lafon, J. Trébosc, F. Deng, and J.-P. Amoureux, "Measurement of hetero-nuclear distances using a symmetry-based pulse sequence in solid-state NMR," *Phys. Chem. Chem. Phys.* **12**, 9395–9405 (2010).
- ⁴⁴X. Lu, O. Lafon, J. Trébosc, and J.-P. Amoureux, "Detailed analysis of the S-RESPDOR solid-state NMR method for inter-nuclear distance measurement between spin-1/2 and quadrupolar nuclei," *J. Magn. Reson.* **215**, 34–49 (2012).
- ⁴⁵N. T. Duong, Z. Gan, and Y. Nishiyama, "Selective ^1H – ^{14}N distance measurements by ^{14}N overtone solid-state NMR spectroscopy at fast MAS," *Front. Mol. Biosci.* **8**, 645347 (2021).
- ⁴⁶B. A. Atterberry, S. L. Carnhahan, Y. Chen, A. Venkatesh, and A. J. Rossini, "Double echo symmetry-based REDOR and RESPDOR pulse sequences for the improved proton detected measurement of heteronuclear dipolar coupling constants," *J. Magn. Reson.* (published online) (2022).
- ⁴⁷H. Nagashima, A. S. Lilly Thankamony, J. Trébosc, F. Pourpoint, O. Lafon, and J. P. Amoureux, " γ -independent through-space hetero-nuclear correlation between spin-1/2 and quadrupolar nuclei in solids," *Solid State Nucl. Magn. Reson.* **84**, 216–226 (2017).
- ⁴⁸J. A. Jarvis, I. M. Haies, P. T. F. Williamson, and M. Carravetta, "An efficient NMR method for the characterisation of ^{14}N sites through indirect ^{13}C detection," *Phys. Chem. Chem. Phys.* **15**, 7613–7620 (2013).
- ⁴⁹J. A. Jarvis, I. Haies, M. Lelli, A. J. Rossini, I. Kuprov, M. Carravetta, and P. T. F. Williamson, "Measurement of ^{14}N quadrupole couplings in biomolecular solids using indirect-detection ^{14}N solid-state NMR with DNP," *Chem. Commun.* **53**, 12116–12119 (2017).
- ⁵⁰J. A. Jarvis, M. Concistre, I. M. Haies, R. W. Bounds, I. Kuprov, M. Carravetta, and P. T. F. Williamson, "Quantitative analysis of ^{14}N quadrupolar coupling using ^1H detected ^{14}N solid-state NMR," *Phys. Chem. Chem. Phys.* **21**, 5941–5949 (2019).
- ⁵¹I. Hung, P. Gor'kov, and Z. Gan, "Efficient and sideband-free ^1H -detected ^{14}N magic-angle spinning NMR," *J. Chem. Phys.* **151**, 154202 (2019).
- ⁵²E. R. H. van Eck, R. Janssen, W. E. J. R. Maas, and W. S. Veeman, "A novel application of nuclear spin-echo double-resonance to aluminophosphates and aluminosilicates," *Chem. Phys. Lett.* **174**, 428–432 (1990).
- ⁵³C. P. Grey and W. S. Veeman, "The detection of weak heteronuclear coupling between spin 1 and spin 1/2 nuclei in MAS NMR; $^{14}\text{N}/^{13}\text{C}/^1\text{H}$ triple resonance experiments," *Chem. Phys. Lett.* **192**, 379–385 (1992).
- ⁵⁴C. P. Grey and A. J. Vega, "Determination of the quadrupole coupling constant of the invisible aluminum spins in zeolite HY with $^1\text{H}/^{27}\text{Al}$ TRAPDOR NMR," *J. Am. Chem. Soc.* **117**, 8232–8242 (1995).
- ⁵⁵D. Carnevale, X. Ji, and G. Bodenhausen, "Double cross polarization for the indirect detection of nitrogen-14 nuclei in magic angle spinning NMR spectroscopy," *J. Chem. Phys.* **147**, 184201 (2017).
- ⁵⁶S. V. Sajith, S. Jayanthi, and A. Lupulescu, "Effective Hamiltonian and ^1H – ^{14}N cross polarization/double cross polarization at fast MAS," *J. Magn. Reson.* **320**, 106832 (2020).
- ⁵⁷J. Trébosc, B. Hu, J. P. Amoureux, and Z. Gan, "Through-space R^3 -HETCOR experiments between spin-1/2 and half-integer quadrupolar nuclei in solid-state NMR," *J. Magn. Reson.* **186**, 220–227 (2007).
- ⁵⁸A. Wong, D. Laurencin, R. Dupree, and M. E. Smith, "Two-dimensional ^{43}Ca – ^1H correlation solid-state NMR spectroscopy," *Solid State Nucl. Magn. Reson.* **35**, 32–36 (2009).
- ⁵⁹A. J. Rossini, M. P. Hanrahan, and M. Thuo, "Rapid acquisition of wide-line MAS solid-state NMR spectra with fast MAS, proton detection, and dipolar HMQC pulse sequences," *Phys. Chem. Chem. Phys.* **18**, 25284–25295 (2016).
- ⁶⁰M. K. Pandey, H. Kato, Y. Ishii, and Y. Nishiyama, "Two-dimensional proton-detected $^{35}\text{Cl}/^1\text{H}$ correlation solid-state NMR experiment under fast magic angle sample spinning: Application to pharmaceutical compounds," *Phys. Chem. Chem. Phys.* **18**, 6209–6216 (2016).
- ⁶¹A. Venkatesh, M. P. Hanrahan, and A. J. Rossini, "Proton detection of MAS solid-state NMR spectra of half-integer quadrupolar nuclei," *Solid State Nucl. Magn. Reson.* **84**, 171–181 (2017).
- ⁶²I. Hung and Z. Gan, "High-resolution NMR of $S = 3/2$ quadrupole nuclei by detection of double-quantum satellite transitions via protons," *J. Phys. Chem. Lett.* **11**, 4734–4740 (2020).
- ⁶³Z. Gan, "Isotropic NMR spectra of half-integer quadrupolar nuclei using satellite transitions and magic-angle spinning," *J. Am. Chem. Soc.* **122**, 3242–3243 (2000).
- ⁶⁴C. Huguenard, F. Taulelle, B. Knott, and Z. Gan, "Optimizing STMAS," *J. Magn. Reson.* **156**, 131–137 (2002).
- ⁶⁵S. E. Ashbrook and S. Wimperis, "Satellite-transition MAS NMR of spin $I = 3/2, 5/2, 7/2,$ and $9/2$ nuclei: Sensitivity, resolution, and practical implementation," *J. Magn. Reson.* **156**, 269–281 (2002).
- ⁶⁶J.-P. Amoureux, C. Huguenard, F. Engelke, and F. Taulelle, "Unified representation of MQMAS and STMAS NMR of half-integer quadrupolar nuclei," *Chem. Phys. Lett.* **356**, 497–504 (2002).
- ⁶⁷F. A. Perras, A. Venkatesh, M. P. Hanrahan, T. W. Goh, W. Huang, A. J. Rossini, and M. Pruski, "Indirect detection of infinite-speed MAS solid-state NMR spectra," *J. Magn. Reson.* **276**, 95–102 (2017).
- ⁶⁸P. Paluch, A. G. M. Rankin, J. Trébosc, O. Lafon, and J.-P. Amoureux, "Analysis of HMQC experiments applied to a spin 1/2 nucleus subject to very large CSA," *Solid State Nucl. Magn. Reson.* **100**, 11–25 (2019).
- ⁶⁹A. Venkatesh, A. Lund, L. Rochlitz, R. Jabbour, C. P. Gordon, G. Menzildjian, J. Viger-Gravel, P. Berruyer, D. Gajan, C. Copéret, A. Lesage, and A. J. Rossini,

- “The structure of molecular and surface platinum sites determined by DNP-SENS and fast MAS ^{195}Pt solid-state NMR spectroscopy,” *J. Am. Chem. Soc.* **142**, 18936–18945 (2020).
- ⁷⁰A. Venkatesh, F. A. Perras, and A. J. Rossini, “Proton-detected solid-state NMR spectroscopy of spin-1/2 nuclei with large chemical shift anisotropy,” *J. Magn. Reson.* **327**, 106983 (2021).
- ⁷¹B. E. G. Lucier, K. E. Johnston, W. Xu, J. C. Hanson, S. D. Senanayake, S. Yao, M. W. Bourassa, M. Srebro, J. Autschbach, and R. W. Schurko, “Unravelling the structure of Magnus’ pink salt,” *J. Am. Chem. Soc.* **136**, 1333–1351 (2014).
- ⁷²X. Lu, O. Lafon, J. Trébosc, G. Tricot, L. Delevoye, F. Méar, L. Montagne, and J. P. Amoureux, “Observation of proximities between spin-1/2 and quadrupolar nuclei: Which heteronuclear dipolar recoupling method is preferable?,” *J. Chem. Phys.* **137**, 144201 (2012).
- ⁷³P. Caravatti, G. Bodenhausen, and R. R. Ernst, “Selective pulse experiments in high-resolution solid state NMR,” *J. Magn. Reson.* **55**, 88–103 (1983).
- ⁷⁴A. Brinkmann and M. H. Levitt, “Symmetry principles in the nuclear magnetic resonance of spinning solids: Heteronuclear recoupling by generalized Hartmann–Hahn sequences,” *J. Chem. Phys.* **115**, 357–384 (2001).
- ⁷⁵A. J. Pell, G. Kervern, L. Emsley, M. Deschamps, D. Massiot, P. J. Grandinetti, and G. Pintacuda, “Broadband inversion for MAS NMR with single-sideband-selective adiabatic pulses,” *J. Chem. Phys.* **134**, 024117 (2011).
- ⁷⁶F. Bloch and A. Siegert, “Magnetic resonance for nonrotating fields,” *Phys. Rev.* **57**, 522–527 (1940).
- ⁷⁷M. Leskes, P. K. Madhu, and S. Vega, “Floquet theory in solid-state nuclear magnetic resonance,” *Prog. Nucl. Magn. Reson. Spectrosc.* **57**, 345–380 (2010).
- ⁷⁸M. H. Levitt, “Why do spinning sidebands have the same phase?,” *J. Magn. Reson.* **82**, 427–433 (1989).
- ⁷⁹A. Jerschow, “From nuclear structure to the quadrupolar NMR interaction and high-resolution spectroscopy,” *Prog. Nucl. Magn. Reson. Spectrosc.* **46**, 63–78 (2005).
- ⁸⁰H.-M. Kao and C. P. Grey, “INEPT experiments involving quadrupolar nuclei in solids,” *J. Magn. Reson.* **133**, 313–323 (1998).
- ⁸¹N. Müller, G. Bodenhausen, and R. R. Ernst, “Relaxation-induced violations of coherence transfer selection rules in nuclear magnetic resonance,” *J. Magn. Reson.* **75**, 297–334 (1987).
- ⁸²M. Bak, J. T. Rasmussen, and N. C. Nielsen, “SIMPSON: A general simulation program for solid-state NMR spectroscopy,” *J. Magn. Reson.* **147**, 296–330 (2000).
- ⁸³M. Bak and N. C. Nielsen, “REPULSION, a novel approach to efficient powder averaging in solid-state NMR,” *J. Magn. Reson.* **125**, 132–139 (1997).
- ⁸⁴S. R. Rabbani, D. T. Edmonds, P. Gosling, and M. H. Palmer, “Measurement of the ^{14}N quadrupole coupling constants in glycine, diglycine, triglycine, and tetraglycine and a comparison with calculation,” *J. Magn. Reson.* **72**, 230–237 (1987).
- ⁸⁵R. E. Stark, R. A. Haberhorn, and R. G. Griffin, “ ^{14}N NMR determination of NH bond lengths in solids,” *J. Chem. Phys.* **68**, 1996–1997 (1978).
- ⁸⁶K. Mao, J. W. Wiench, V. S.-Y. Lin, and M. Pruski, “Indirectly detected through-bond chemical shift correlation NMR spectroscopy in solids under fast MAS: Studies of organic–inorganic hybrid materials,” *J. Magn. Reson.* **196**, 92–95 (2009).
- ⁸⁷R. K. Harris, E. D. Becker, S. M. Cabral de Menezes, R. Goodfellow, and P. Granger, “NMR nomenclature. Nuclear spin properties and conventions for chemical shifts,” *Pure Appl. Chem.* **73**, 1795–1818 (2001).
- ⁸⁸A. Sasaki, J. Trébosc, and J.-P. Amoureux, “Accelerating the acquisition of high-resolution quadrupolar MQ/ST-HETCOR 2D spectra under fast MAS via ^1H detection and through-space population transfers,” *J. Magn. Reson.* **333**, 107093 (2021).
- ⁸⁹B. E. G. Lucier, A. R. Reidel, and R. W. Schurko, “Multinuclear solid-state NMR of square-planar platinum complexes—Cisplatin and related systems,” *Can. J. Chem.* **89**, 919–937 (2011).
- ⁹⁰M. Pons, M. Feliz, and E. Giral, “Steady-state DQF-COSY spectra using a variable relaxation delay,” *J. Magn. Reson.* **78**, 314–320 (1988).
- ⁹¹D. Marion, M. Ikura, R. Tschudin, and A. Bax, “Rapid recording of 2D NMR spectra without phase cycling. Application to the study of hydrogen exchange in proteins,” *J. Magn. Reson.* **85**, 393–399 (1989).
- ⁹²D. Corinti, C. Coletti, N. Re, S. Piccirillo, M. Giampà, M. E. Crestoni, and S. Fornarini, “Hydrolysis of cis- and transplatin: Structure and reactivity of the aqua complexes in a solvent free environment,” *RSC Adv.* **7**, 15877–15884 (2017).
- ⁹³M. J. Hunt and A. L. Mackay, “Deuterium and nitrogen pure quadrupole resonance in amino acids. II,” *J. Magn. Reson.* **22**, 295–301 (1976).